Daytime variation of aerosol indirect effect for warm marine boundary layer clouds in the eastern north Atlantic

Shaoyue Qiu[1], Xue Zheng[1], David Painemal[2,3], Christopher R. Terai[1], and Xiaoli Zhou[4,5]

[1]Atmospheric, Earth and Energy Division, Lawrence Livermore National Laboratory, Livermore, California, USA
[2] Science Directorate, NASA Langley Research Center, Hampton, VA, USA
[3] Analytical Mechanics Associates, Hampton, VA, USA
[4]Chemical Sciences Laboratory, NOAA, Boulder, CO, USA,
[5]Cooperative Institute for Research in Environmental Sciences (CIRES), University of Colorado, Boulder, CO, USA

Correspondence to: Shaoyue Qiu (qiu4@llnl.gov)

Abstract. Warm boundary layer clouds in the Eastern North Atlantic region exhibit significant diurnal variations in cloud properties. However, the diurnal cycle of the aerosol indirect effect (AIE) for these clouds remains poorly understood. This study takes advantage of recent advancements in the spatial resolution of geostationary satellites to explore the daytime variation of AIE by estimating the cloud susceptibilities to changes in cloud droplet number concentration (N_d). Cloud retrievals for four months of July (2018-2021) from SEVIRI on Meteosat-11 over this region are analyzed. Our results reveal a significant "U-shaped" daytime cycle in susceptibilities of cloud liquid water path (LWP), cloud albedo, and cloud fraction. Clouds are found to be more susceptible to N_d perturbations at noon and less susceptible in the morning and evening. The magnitude and sign of cloud susceptibilities depend heavily on the cloud state defined by cloud LWP and precipitation conditions. Non-precipitating thin clouds account for 44% of all warm boundary layer clouds in July and they contribute the most to the observed daytime variation. Non-precipitating thick clouds are the least frequent cloud state (10%), they exhibit more negative LWP and albedo susceptibilities compared to thin clouds. Precipitating clouds are the dominant cloud state (46%), but their cloud susceptibilities show minimal variation throughout the day.

We find evidence that the daytime variation of LWP and albedo susceptibilities for non-precipitating clouds are influenced by a combination of the diurnal transition between non-precipitating thick and thin clouds and the "lagged" cloud responses to N_d perturbations. The daytime variation in cloud fraction susceptibility for non-precipitating thick clouds can be attributed to the daytime variation in cloud morphology (e.g., overcast or broken). The dissipation and development of clouds do not adequately explain the observed variation in cloud susceptibilities. Additionally, daytime variation of cloud susceptibility is primarily driven by variation in the intensity of cloud response rather than the frequency of occurrence of cloud states. Our results imply that polar-

38   orbiting satellites with overpass time at 13:30 local time underestimate daytime mean value of cloud susceptibility,

39   as they observe susceptibility daily minima in the study region.

40

41

1. Introduction

Warm boundary layer clouds, including stratus, stratocumulus, and cumulus clouds, are prevalent over the sub-tropical oceans, account for over 30% of the global annual mean cloud coverage (Warren et al., 1988; Wood, 2012). These clouds have a significant net negative radiative forcing on the surface radiation budget. However, our understanding of the aerosol indirect effect (AIE) on these clouds, particularly the impact of aerosols on cloud amount, brightness, and lifetime, remains a significant source of uncertainty in estimating the radiative forcing from human activities. The AIE plays a critical role in the Earth's radiation budget through its interactions with clouds. It consists of two effects: the Twomey effect, which involves the increase in cloud droplet number from increasing aerosols, and leads to an increase in cloud albedo (α_c) from smaller droplets when the cloud liquid water path (LWP) is held constant (Twomey, 1977), and the cloud adjustment effect, which encompasses the impact of aerosols on cloud amount, cloud water, and α_c through modulating cloud processes (e.g., Albrecht, 1989; Xue and Feingold, 2006; Chen et al., 2014; Gryspeerdt et al., 2019). The cloud adjustment effect is highly variable with large uncertainties in signs and magnitudes depending on cloud state, boundary layer, and meteorological conditions among other factors (e.g., Han et al., 2002; Wang et al., 2003; Small et al., 2009; Sato et al, 2018).

Previous studies have made significant progress in identifying different cloud processes and feedback mechanisms to explain the responses of CF, LWP, and α_c to aerosol perturbations (e.g., as summarized in Steven and Feingold, 2009; Fan et al., 2016; Gryspeerdt et al., 2019). The cloud adjustment effect is influenced by two key feedback mechanisms: precipitation suppression, and sedimentation-evaporation-entrainment.

Under clean conditions and for clouds predominantly precipitating, an increase in the cloud droplet number concentration (N_d) and associated decrease in droplet sizes, reduces precipitation efficiency, and decreases water loss from precipitation. Consequently, this promotes an increase in cloudiness and cloud LWP (Albrecht, 1989; Qian et al., 2009; Li et al., 2011; Terai et al., 2012, 2015). For non-precipitating clouds, decreased cloud drop size due to increases in N_d impacts CF and LWP through their impact on the entrainment rate. A decrease in cloud droplet size diminishes the sedimentation rate in clouds, causing an accumulation of cloud water near the cloud top. This increased cloud water in the entrainment zone enhances cloud-top radiative cooling, entrainment rate, and evaporation, resulting in a decrease in CF and cloud LWP (Bretherton et al., 2007; Chen et al., 2014; Toll et al., 2019; Gryspeerdt et al., 2019).

Additionally, the faster evaporation rates from smaller droplets enhance cloud-top cooling, downward motion in clouds, total kinetic energy, and horizontal buoyancy gradient. The processes listed above, in turn, increase evaporation and entrainment rate and, thus, forming a positive feedback loop (Wang et al., 2003; Xue and Feingold, 2006; Small et al., 2009; Toll et al., 2019). Furthermore, among non-precipitating clouds, thick clouds with larger LWP exhibit stronger cloud-top longwave radiative cooling rate and therefore stronger cloud-top entrainment rate (e.g., Sandu et al., 2008, Williams and Igel, 2021). Therefore, the classification of cloud states (e.g., precipitating conditions and thickness) is essential for accurately quantifying the AIE and discerning opposing cloud processes. In this study, we classify cloud states based on the LWP-N_d parameter space, as these variables provide the most informative metrics for cloud susceptibility (Zhang et al., 2022).

78   This study focuses on the Eastern North Atlantic (ENA) region, where the U.S. Department of Energy
79   (DOE) Atmospheric Radiation Measurement program (ARM) deployed the ground-based user facility at the Azores
80   archipelago (Mather and Voyles, 2013). During the summer over ENA region, warm boundary layer clouds exhibit
81   pronounced diurnal variations in their properties and cloud states. For example, based on ARM surface radar and
82   lidar observations, the frequency of stratocumulus clouds is highest at night, accompanied by an increase in the
83   fraction of precipitating clouds. Throughout the daytime, both cloud fraction and precipitation fraction experience a
84   slight decrease, followed by an increase after sunset (Remillard et al, 2012). The retrieved cloud microphysical
85   properties from ARM ground-based observations show similar "U-shaped" diurnal variations in cloud LWP, liquid
86   water content, and optical thickness (Dong et al., 2014). Additionally, numerical studies have revealed a distinct
87   diurnal cycle of AIE for marine stratocumulus clouds, attributed to changes in cloud properties and boundary layer
88   thermodynamic conditions (e.g., Sandu et al., 2008, 2009). However, observational analyses based on the ground-
89   based observations at the ENA site or in-situ measurements from field campaigns are often based on a few cases
90   with limited samples and insufficient spatial coverage (e.g., Liu et al., 2016; Wang et al., 2021; Zheng et al., 2022).
91   There have been few observational studies investigating the diurnal cycle of AIE in the ENA region. With recent
92   advancements in the spatial resolution of geostationary satellites, this study aims to investigate the diurnal variation
93   of the AIE in warm boundary layer clouds over the ENA region and gain a better understanding of the underlying
94   mechanisms.

95   Both cloud properties and meteorological conditions have substantial spatiotemporal variability and distinct
96   diurnal variations. Furthermore, changes in meteorological conditions can in turn influence cloud and aerosol
97   properties. One of the main challenges in understanding the AIE lies in isolating the impacts of the confounding
98   meteorological drivers on clouds and aerosols from AIE on clouds. To address this challenge, Gryspeerdt et al.
99   (2016) proposed the use of N_d as an intermediary variable for AIE, instead of using aerosol optical depth (AOD) or
100   aerosol index. The use of N_d circumvents the well-known dependency of AOD on CF and surface wind speed,
101   which does not necessarily reflect actual changes in aerosol loading. Moreover, the control of relative humidity and
102   aerosol type on AOD prevents to establish a direct link between AOD and aerosol concentration or cloud
103   condensation nuclei (CCN).

104   Another common method to disentangle meteorological impacts is to sort the controlling meteorological
105   factors of cloud state, such as relative humidity, lower tropospheric stability, vertical velocity, and examine the AIE
106   accordingly (e.g., Chen et al., 2014; Gryspeerdt et al., 2019). However, this approach overlooks important
107   information, including the frequency of occurrence of specific environmental conditions, the spatiotemporal co-
108   variation of meteorological factors, and the correlations among them. Zhou et al. (2021) and Zhang et al. (2022)
109   proposed a new method to estimate the cloud susceptibility within a confined space (e.g., a 1° × 1° or 2° × 2° grid
110   box) of each satellite snapshot by assuming consistent meteorological conditions within this spatial domain.
111   Additionally, it is important to note that meteorological conditions influence albedo susceptibility by altering the
112   frequency of occurrence of different cloud states (e.g., precipitating and non-precipitating). Specifically, within a
113   particular cloud state, meteorological conditions offer limited information regarding cloud susceptibility (Zhang et
114   al, 2022).

115   The second main source of uncertainty in observational AIE studies arise from inferring processes in a

116   temporally evolving system based on snapshots of observations (Mülmenstädt and Feingold, 2018). Due to the

117   limited temporal or spatial resolution of the observations, most studies assume a Markovian system, where clouds

118   and AIE are assumed to only relate to the current state of the system and have no memory of the past states.

119   However, this assumption contradicts the nature of the cloud system. Observational and modeling studies have

120   shown that aerosol-cloud interaction processes take hours to reach the equilibrium state and the sensitivity of AIE is

121   time dependent. For instance, Glassmeier et al. (2021) applied a Gaussian-process emulation and derived the

122   adjustment equilibration timescale for LWP to be ~20 hours. By tracking the ship tracks in satellite observations,

123   Gryspeerd et al. (2021) found a similar AIE timescale of ~20 hours or longer and the magnitude of LWP

124   susceptibility increases with time. In addition, Christensen et al. (2020) discovered that influence of aerosols on

125   cloud LWP, CF, and cloud top height persists two to three days by tracking cloud systems in satellite observations.

126   In summary, the sensitivity of cloud responses to N_d perturbations changes with time and, thus, the assumption that

127   AIE has no memory of its past state is inadequate. Nonetheless, the direct evaluation of the impact of cloud memory

128   on the quantified cloud susceptibility remains unexplored, to the best of our knowledge.

129   To facilitate a process-level understanding of the drivers behind the diurnal variation of AIE for warm

130   boundary layer clouds, we will classify these clouds into three states: precipitating clouds, non-precipitating thick

131   clouds, and non-precipitating thin clouds. We investigate the changes in both the frequency of occurrence of cloud

132   states and the magnitude of AIE for different cloud states throughout the day. Additionally, we document the

133   temporal changes in cloud state within each fixed 1° × 1° grid box and quantify the influences of cloud memory and

134   state transition on AIE. Section 2 describes the datasets as well as the methodology employed to quantify cloud

135   susceptibilities, distinguish precipitating clouds from the satellite retrievals, and track cloud states. We present our

136   results in Section 3. Section 3.1 characterizes the general conditions of warm boundary clouds over the ENA region

137   during the summer. Section 3.2 introduces the LWP-N_d parameter space and illustrates the dependence of cloud

138   responses to N_d perturbations on cloud states. We then discuss the mean daytime variation of cloud susceptibilities

139   for all cloud states in Section 3.3, followed by an analysis of the AIE daytime variation for each cloud state and the

140   impact of the state transition on AIE in Section 3.4. In Section 3.5, we decompose the contributions to the daytime

141   variation of cloud susceptibility into two components, one is from changes in the frequency of occurrence of

142   different cloud states and the other is from changes in the intensity of AIE during the day. Section 4 includes

143   discussions on the similarities and differences in findings between this study and previous studies of AIE and

144   Section 5 is the summary and conclusions of this study.

145   **2. Dataset and Methodology**

146   We use cloud retrievals derived from the Spinning Enhanced Visible InfraRed Imager (SEVIRI) on

147   Meteosat-11, with a spatial resolution of 3 km at nadir and a half-hourly temporal resolution over the ENA region

148   (33-43°N, 23-33°W). SEVIRI cloud products are derived using the Satellite ClOud and Radiation Property retrieval

149   System (SatCORPS) algorithms (e.g., Painemal et al., 2021), based on the methods applied by the Clouds and the

150 Earth's Radiant Energy System (CERES) project, and specifically tailored to support the ARM program over the

151 ARM ground-based observation sites (Minnis et al. 2011, 2020). Given the purpose of this study on quantifying the

152 AIE on warm boundary layer clouds, we focus on four months of July (2018-2021), a period that coincides with the

153 highest frequency of occurrence of warm boundary layer clouds over the ARM ENA site (Rémillard et al. 2012;

154 Dong et al., 2014, 2023).

155   The cloud mask algorithm implemented in SatCORPS is described in Trepte et al. (2019). SatCORPS cloud

156 properties are based on the shortwave-infrared split-window technique during daytime (VISST, Minnis et al. 2011,

157 2020), with cloud optical depth (τ) and effective radius (r_e) being derived using an iterative process that combines

158 reflectance and brightness temperatures from the 0.64 μm and 3.9 μm channels. Cloud LWP is computed from τ and

159 r_e using the formula $LWP = \frac{4r_e\tau}{3Q_{ext}}$, where Q_{ext} represents the extinction efficiency and assumed constant of 2.0

160 (Minnis et al. 2011, 2020). The top-of- atmosphere (TOA) broadband shortwave α_c is derived from an empirical

161 radiance-to-broadband conversion using the satellite imager's visible channel and CERES Single Scanning Footprint

162 (SSF) shortwave fluxes, and dependent on solar zenith angle and surface type (Minnis et al. 2016). Cloud top height

163 computation follows the methodology in Sun-Mack et al. (2014).

164   To validate the Meteosat-11 retrieved cloud mask and the detection of boundary layer clouds, we compare

165 the boundary layer cloud fractions derived from Meteosat-11 with the ground-based observations at the ARM ENA

166 site. As seen in Fig.S1, both the diurnal variation and the mean CF of Meteosat-11 agree well with ARM

167 observations. More details on the methodology for the evaluation study are included in the supplementary material.

168   Our analysis focuses on warm boundary layer clouds with cloud tops below 3km and a liquid cloud phase.

169 To focus specifically on boundary layer cloud cases without including the edges of deep clouds, we apply a stricter

170 threshold than merely using the pixel-level cloud top height. We define boundary layer clouds as those with 90% of

171 their cloud tops below 3km, labeling all contiguous cloudy pixels as distinct cloud objects.

172   Cloud N_d is retrieved based on the adiabatic assumptions for warm boundary layer clouds, as in Grosvenor

173 et al. (2018) according to the following equation:

$$N_d = \frac{\sqrt{5}}{2\pi k}\left(\frac{f_{ad}c_w\tau}{Q_{ext}\rho_w r_e^5}\right)^{1/2} \qquad (1)$$

175 In Equation (1), k represents the ratio between the volume mean radius and r_e, assumed to be constant of 0.8 for

176 stratocumulus; f_{ad} is the adiabatic fraction of the observed liquid water path and assumed to be 0.8 for

177 stratocumulus clouds (Brenguier et al., 2011; Zuidema et al., 2012); c_w is the condensation rate, which is a function

178 of temperature and pressure; Q_{ext} is the extinction coefficient, approximated as 2 in this study; and ρ_w is the density

179 of liquid water. While the different components of Eq. (1) could contribute to the uncertainties in N_d, errors in r_e are

180 the dominant drivers in Eq. (1) (Grosvenor et al., 2018).

181   To minimize uncertainties associated with bias in satellite cloud microphysical retrievals, we only select

182 pixels with a minimum r_e of $3\mu m$, a minimum τ of 3, and a solar zenith angle (SZA) of less than 65° (e.g., Painemal

183 et al., 2013; Painemal, 2018; Zhang et al., 2022). The SZA threshold of 65° was chosen to minimize biases observed

184 at high solar zenith angle in r_e and τ (e.g., Grosvenor & Wood, 2014; Grosvenor et al., 2018).

185   In addition, to reduce uncertainties associated with the adiabatic assumption in the N_d retrieval, we

186   implement a filtering process. For each cloud, we exclude cloudy pixels at the cloud edge, defined as those adjacent

187   to cloud-free pixels, following a similar sampling strategy suggested by Gryspeerdt et al. (2022). Therefore, all

188   cloud properties in this study refer to the properties of cloud body without cloud edge. It is worthy of note that

189   shallow cumulus clouds with diameters smaller than 9km are not included. The removal of cloud-edge pixels

190   accounts for ~14% of the cloudy pixels. Furthermore, we removed grid boxes containing islands due to the

191   uncertainties in Meteosat retrievals over contrasting underlying surface. Lastly, to avoid unrealistically large

192   retrievals, we eliminate pixels with the retrieved N_d values exceeding 1000 cm^{-3}, which constituted only 0.002% of

193   the data.

194   Cloud susceptibility is quantified as the slope between cloud properties and N_d using a least-square

195   regression. As found by Arola et al. (2022) and Zhou and Feingold (2023), the retrieved cloud susceptibilities are

196   sensitive to small-scale cloud heterogeneity, the co-variability between cloud properties and N_d, and the spatial scale

197   of cloud organization. To reduce biases resulting from heterogeneity and co-variability, we first average the 3-km

198   pixel-level cloud retrievals and N_d (Eq. 1) to a regular 0.25° × 0.25° grid for each half-hourly time step.

199   To further mitigate the impact from co-variability between cloud properties and N_d at larger spatiotemporal

200   scales, cloud susceptibility is estimated within a 1° × 1° grid box at each satellite time step (e.g., Zhang et al, 2022).

201   Moreover, estimating the cloud susceptibility over a confined space also help to constrain the meteorological

202   impacts on AIE, with the assumption of a homogeneous meteorological condition within this spatial scale. Next,

203   susceptibilities are calculated using the 0.25° smoothed data if the number of data points within the 1° × 1° box

204   exceeds six (from a maximum of 16 data points). It is important to note that when computing the 0.25° × 0.25°

205   averaged cloud properties, only data from cloudy pixels are used to ensure that the estimated susceptibility is not

206   weighted by CF or impacted by satellite artifacts. Lastly, due to the minimal spatial variability of cloud

207   susceptibility in the study region, the 1° cloud susceptibility is averaged over the study region (33-43°N, 23-33°W)

208   to characterize the daytime variation of AIE. Additionally, results and conclusions of this study are not sensitive to

209   the size of the box calculating the cloud susceptibility (e.g., over a 0.8° × 0.8° box or over a 1.5° × 1.5° box, not

210   shown).

211   Because of the nonlinear relationships between LWP and N_d, the LWP susceptibility is defined as the slope

212   in logarithmic scale, that is: $dln(LWP)/dln(N_d)$ (e.g., Gryspeerdt et al. 2019). The albedo susceptibility is

213   estimated as the slope between α_c and ln (N_d), equivalent to $d\alpha_c/dln(N_d)$ (e.g., Painemal 2018). Lastly, the CF

214   susceptibility is estimated as $dCF/dln(N_d)$. The mean CF is defined as the fraction of cloudy pixels excluding

215   cloud edge to the sum of cloudy and clear pixels within each 0.25° × 0.25° box. Due to the highly variable nature of

216   CF, the variability in the 0.25° CF could arise from quantifying edges or centers of the same cloud layer rather than

217   N_d perturbations. To assess the potential influence of cloud morphology on the retrieved CF susceptibility, we

218   excluded any 1° × 1° scene meeting the following three criteria: 1) the difference between the maximum and

219   minimum 0.25° CF greater than 0.9, 2) the variation in the 0.25° N_d less than 60 cm^{-3}, and 3) the 0.25° CF in the

220   1° × 1° box sample the same cloud. The 0.9 and 60 cm^{-3} thresholds represent ~45% of the data. With the three

221   thresholds combined, a total of 17,000 scenes were removed, which accounts for ~24% of the total samples.

222 Removing these scenes does not change the conclusions of CF susceptibility in this study (not shown), which

223 demonstrates that cloud morphology, has minimal impact on the retrieved CF susceptibility. Furthermore, as we

224 removed N_d retrievals at cloud edge where N_d likely suffers large uncertainties, cloudy pixels at cloud edge are set

225 as clear for consistency in the calculation of the CF susceptibility. Removing the cloud edge decreases the four-

226 month mean CF for warm boundary layer clouds from 21.6% to 19.0%.

227 The susceptibility of the shortwave radiative fluxes to N_d (F_0) is estimated as the sensitivity of the TOA

228 shortwave upward radiative flux (SW_{TOA}^{up}) to N_d perturbations (e.g., Chen et al. 2014; Painemal 2018; Zhang et al.

229 2022). The mean SW_{TOA}^{up} over a $1° \times 1°$ grid box is estimated using Eq. (2), with the assumption that the clear-sky

230 albedo over the ocean is small compared to the cloud albedo:

231
$$\overline{SW_{TOA}^{up}} = \overline{SW_{TOA}^{dn}} \cdot \overline{\alpha_c} \cdot \overline{CF}, \tag{2}$$

232 where SW_{TOA}^{dn} is the grid-box mean TOA shortwave downward radiative flux, which is estimated based on the

233 latitude, longitude, date, and overpass time of each pixel, α_c and CF are the grid-box mean values. Then, F_0 is

234 estimated using the calculated α_c and CF susceptibilities, and the $1° \times 1°$ grid-box mean cloud properties as shown

235 in the equation below:

236
$$F_0 = -\frac{dSW_{TOA}^{up}}{dln(N_d)} = -\overline{SW_{TOA}^{dn}} \cdot \left(\frac{d\alpha_c}{dln(N_d)} \cdot \overline{CF} + \frac{dCF}{dln(N_d)} \cdot \overline{\alpha_c}\right). \tag{3}$$

237 F_0 is in the unit of $W\ m^{-2}\ ln\ (N_d)^{-1}$, and a positive value indicates a decrease in the SW_{TOA}^{up}, which is a *warming*

238 effect at the surface.

239 To minimize uncertainties in the linear regression for the estimated susceptibility, we analyze regressions

240 that exhibited a goodness of fit exceeding the 95% confidence interval (i.e., $\chi^2 < \chi_{0.95,c}^2$), and an absolute

241 correlation coefficient greater than 0.2 (e.g., Painemal, 2018; Zhang et al., 2022). There is a total of ~115,000

242 samples of the 1° cloud susceptibilities in this study, applying the goodness of fit thresholds result in exclusions of ~

243 33,000- 43,000 samples for different susceptibilities, which are ~28-37% of the data. Sensitivity test shows that

244 including cases that fail the goodness of fit test will not change the results and conclusions of this study (not shown).

245 Specifically, including these cases decrease the magnitude of cloud susceptibilities for all three cloud states, but the

246 signs of cloud responses to N_d perturbations remain consistent.

247 Since precipitating and non-precipitating clouds exhibit distinct responses to aerosol perturbations due to

248 the effect of precipitation suppression and the wet-scavenging feedback, it is critical to distinguish between these

249 two cloud states when estimating AIE. Previous studies have utilized various methods based on the effective radius

250 threshold (e.g., Gryspeerdt et al., 2019, Toll et al., 2019; Zhang et al., 2022) and the rain rate threshold (e.g., Duong

251 et al., 2011; Terai et al., 2015) from satellite retrievals. In our study, we validate these two methods using the

252 precipitating mask estimated from ground-based observations with a radar reflectivity threshold together with the

253 lidar-defined cloud base at the ARM ENA site (e.g., Wu et al., 2020). The thresholds of $r_e > 12\ \mu m$ and $r_e > 15\ \mu m$

254 yield hit rates of 0.79 and 0.73, respectively. However, the false alarm rate is higher for $r_e > 12\ \mu m$ (0.21) compared

255 to $r_e > 15\ \mu m$ (0.1). Rain rate is computed using the empirical relationships derived from ground-based

256 measurements in Comstock et al. (2004) as $R = 0.0156\ (^{LWP}/_{N_d})^{1.75}$. Using a threshold of R>0.05 mm/h results

257 in a hit rate of 0.65. Consequently, we use the $r_e > 15\ \mu m$ threshold to define precipitating clouds in this study.

To investigate the dependences of cloud susceptibility on previous cloud states and quantify the influence of cloud memory on the estimated cloud susceptibility, we track the historical cloud state over a 1° × 1° grid box for a two-hour period. During the summer in the study region, low wind conditions prevail in the boundary layer, with the mean wind speed being less than 10 m/s for 85% of the time and less than 7 m/s for 60% of the time. Therefore, in most cases, less than half of the clouds exit the grid box within the two hours, allowing us to track the previous cloud state within the same grid box (i.e., from the~~an~~ Eulerian perspective). The influence of cloud memory is assessed by comparing the cloud susceptibilities of clouds that undergo a transition in cloud state with those that do not experience such a transition. Section 3.4 provides more details and discussion on the sensitivity of tracking time and the influence of advection on our classification.

3. Results

3.1 General cloud conditions and mean cloud responses to N_d perturbations

In the ENA region, characterized by dominant Bermuda High with its prevailing ridge and zonal synoptic pattern (Mechem et al., 2018), the summer season gives rise to the annual peak in boundary layer cloud coverage The monthly mean low-level CF retrieved from Meteosat-11 reaches its maximum of 35% in July, compared to an annual mean of 17% during the four-year study period. This region represents a typical clean marine condition, situated far from continental influences, which results in a consistently low N_d compared to polluted marine regions, such as the northeastern (NE) Pacific near California or the northwestern Atlantic near the Gulf of Maine. In July, the mean N_d over the ENA region is 65 cm^{-3} with the lower 5th and upper 95th percentile of 15 and 160 cm^{-3}, respectively. The retrieved N_d values in this study closely align with in-situ measurements from the Aerosol and Cloud Experiments in Eastern North Atlantic (ACE-ENA) field campaign. For instance, the in-situ measured N_d in July 2017 varied from 25 to 150 cm^{-3}, with a mean value of 65 cm^{-3} (e.g., Yeom et al., 2021; Zhang et al., 2021). Moreover, our satellite retrieved N_d exhibits good agreement with retrievals based on ground-based observations at the ARM ENA site (e.g., Dong et al., 2014; Wu et al., 2020) and the MOderate resolution Imaging Spectroradiometer (MODIS, e.g., Bennartz 2007; Bennartz and Rausch 2017).
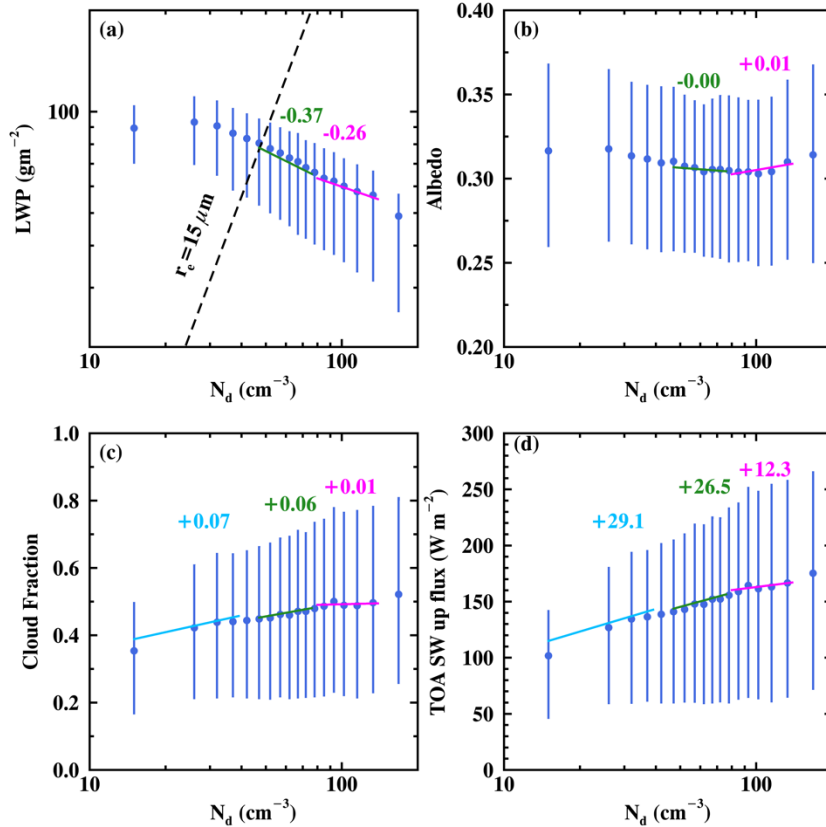
Figure 1. Relationships between N_d and cloud properties: (a) cloud LWP, (b) cloud albedo, (c) cloud fraction, and (d) TOA shortwave upward radiative flux. The dots represent the mean values, while the whiskers indicate the upper and lower 25th percentile. In (a), the dashed line denotes $r_e = 15\ \mu m$, serving as an indicator of precipitation occurrence, with precipitating clouds located to the left of the line. Blue, green, and magenta lines in panels (a)-(d) represent the regression slopes of the mean cloud properties, and the mean $ln(N_d)$, for $N_d < 40\ cm^{-3}$, N_d between 40 and 80 cm^{-3}, and $N_d > 80\ cm^{-3}$, respectively.

Previous studies have demonstrated that clouds exhibit diverse responses to aerosol perturbations under clean and polluted conditions (e.g., Fan et al. 2016; Mülmenstädt and Feingold, 2018). Figure 1 shows the relationships between the climate mean cloud properties, derived from the pixel-level SEVIRI cloud products, and averaged to the 1° × 1° resolution, as a function of the 1° × 1° mean N_d values. To quantify these responses, cloud susceptibility is estimated as the slope of the mean cloud variable changes across N_d bins. In pristine conditions (N_d < 40 cm^{-3}, ~28% of data), clouds predominantly precipitate (r_e >15 μm, Fig.1a). The mean cloud LWP features a slight increase followed by a decrease with increasing N_d. This result departs from the precipitation suppression hypothesis, in which LWP typically increases. The absence of a precipitation suppression signal is likely attributed to the relatively modest precipitation that occurs in this region during summer (e.g., Wu et al., 2020; Zheng and Miller, 2022), resulting in a minimal precipitation suppression effect and a dominant entrainment drying effect. In terms of α_c, the potential decrease in α_c attributed to a LWP reduction offsets the potential increases in α_c caused by the Twomey effect, resulting in a net zero change in mean α_c for clouds with N_d < 40 cm^{-3} (Fig.1b). Furthermore, the majority of precipitating clouds are broken, with a mean CF that increases with N_d from 0.35 to 0.45 (Fig.1c). Consequently, the mean SW_{TOA}^{up} flux increases from 100 to 140 $W\ m^{-2}$ as N_d increases from 10 to 40 cm^{-3}. This

303   increase in CF for precipitating clouds aligns with previous study over the north Atlantic region across all seasons

304   (e.g., Gryspeerdt et al., 2016). In summary, despite the slight decrease in mean LWP with increasing N_d for

305   precipitating clouds, the mean cloud albedo remains relatively constant, while the mean CF increases, resulting in an

306   overall increase in the TOA reflected shortwave flux.

307   Under relatively polluted conditions with $N_d > 40\ cm^{-3}$ (~72% of data), the mean LWP shows a

308   decreasing trend with N_d. For N_d values between 40-80 cm^{-3}, the ln(LWP)- $ln(N_d)$ slope is -0.37, while for N_d

309   exceeding 80 cm^{-3}, the slope reaches -0.26 (green and magenta lines in Fig.1a). This negative adjustment of LWP

310   for non-precipitating clouds is consistent with the sedimentation-evaporation-entrainment feedback, as well as with

311   previous studies of stratocumulus clouds in other regions (e.g., Gryspeerdt et al., 2019; Zhang et al., 2022). The

312   mean α_c remains nearly constant within the N_d range of 40-80 cm^{-3} (Fig.1b). As LWP decreases at a slower rate

313   for N_d >80 cm^{-3}, the Twomey effect becomes more dominant and leads to a slight increase in α_c with a slope of

314   0.01 (magenta line in Fig.1b). For non-precipitating clouds, the mean CF slightly increases with increasing N_d with

315   a CF susceptibility of 0.06 and 0.01 (green and magenta lines in Fig.1c). As a result, the SW_{TOA}^{up} flux exhibits a

316   weaker susceptibility compared to precipitating clouds (Fig.1d).

317   **3.2 Daytime mean cloud susceptibilities in the LWP-N_d space**

318   One limitation of the relationships derived from the mean cloud properties with sorted N_d is the

319   confounding effect from meteorological impacts on cloud properties and cloud susceptibilities. As a comparison,

320   Fig.2 shows the mean cloud susceptibility estimated within each half-hourly snapshot's $1° \times 1°$ grid box and

321   averaged in the LWP-N_d parameter space. There are around 72,000-82,000 samples of the 1° cloud susceptibilities

322   in this study. The number of samples for different cloud susceptibilities are slightly different due to the goodness of

323   fit test for each regression. We calculate the mean susceptibilities for LWP-N_d bins with more than 100 cloud

324   susceptibility samples. Blank bins in Fig.2 are bins with less than 100 samples. Figure 2e shows the occurrence

325   frequency of samples for the LWP susceptibility in Fig.2a.

326   With the assumption that the meteorological condition is homogeneous in each grid box, the estimated

327   cloud susceptibilities exhibit much stronger relationships for all cloud variables compared to the climatological

328   mean adjustment rates shown in Fig.1. The disparities between the two methods suggest that meteorological

329   confounders tend to obscure the signal of the AIE over the ENA region. Moreover, the cloud responses for both

330   precipitating and non-precipitating clouds exhibit consistent signs between the half-hourly (Fig.2) and

331   climatological-mean approaches (Fig.1). This consistency is likely attributed to the confined domain (a $10° \times 10°$)

332   and the focus on July in this study, which limit the spatial and temporal covariability between cloud properties and

333   N_d. This consistency also demonstrates that the overall cloud responses to N_d perturbations primarily depend on

334   cloud states (e.g., precipitating conditions and cloud thickness).

335   The dependence of cloud response on cloud state is illustrated in Fig.2. We define three cloud states*: (1)

336   *the precipitating clouds (r_e>15 μm),(2) the non-precipitating thick clouds (r_e<15 μm, LWP > 75 gm^{-2}),* and (3)

337   *the non-precipitating thin clouds (r_e<15 μm, LWP < 75 gm^{-2}),* similar to the definition in Zhang et al. (2022).
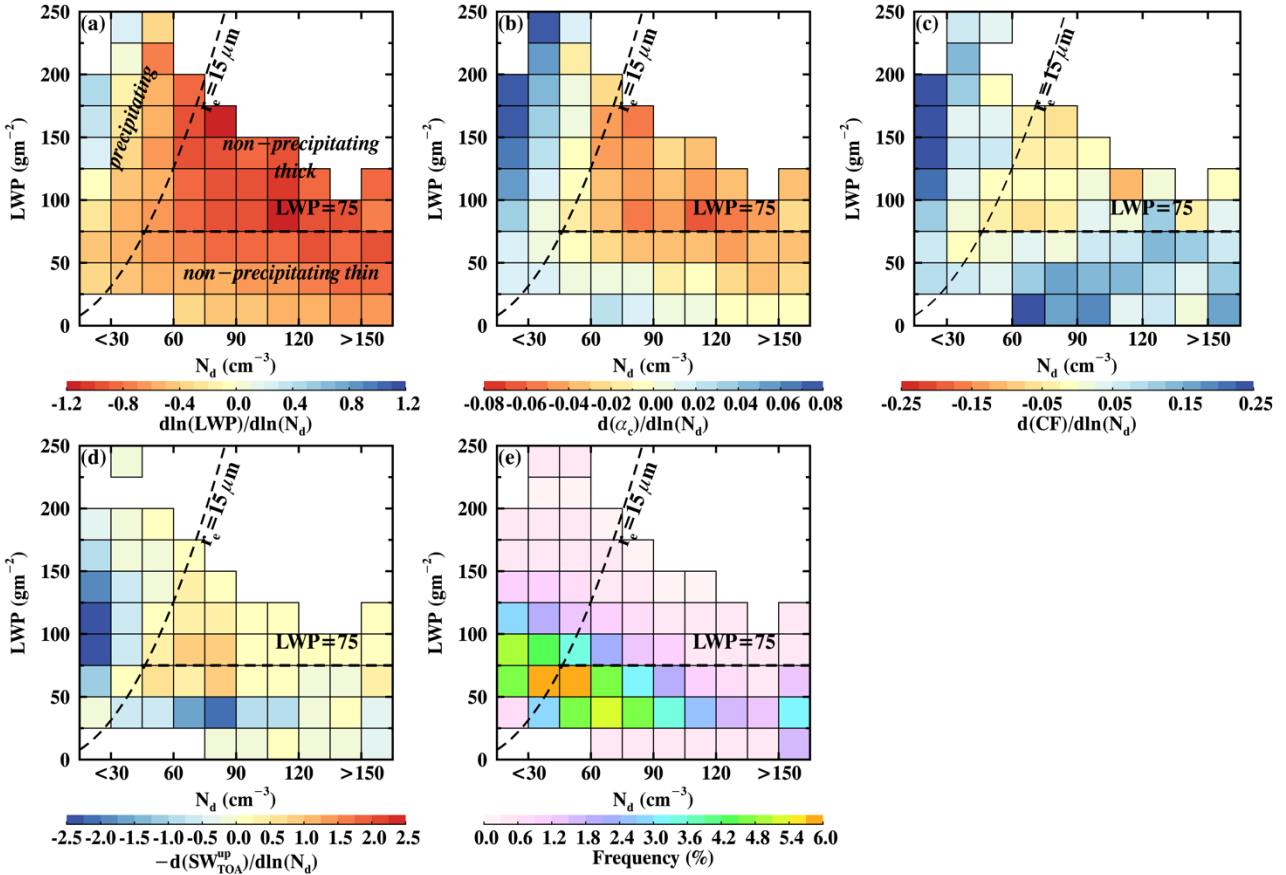
Figure 2. Mean cloud susceptibilities for different N_d and LWP bins during the daytime. (a) cloud LWP susceptibility ($dln(LWP)/dln(N_d)$), (b) cloud albedo susceptibility ($d\alpha_c/dln(N_d)$), (c) cloud fraction susceptibility ($dCF/dln(N_d)$), (d) cloud shortwave susceptibility ($-dSW_{TOA}^{up}/dln(N_d)$) weighted by the frequency of occurrence of samples of each bin, and (e) frequency of occurrence of samples in each bin. The dashed lines in (a)-(e) indicate $r_e = 15\ \mu m$ and LWP= 75 gm^{-2}, as thresholds for precipitation (precipitating clouds located to the left of the line) and thick clouds (with LWP > 75 gm^{-2}). The defined three clouds states are noted in (a).

a. Precipitating clouds

Among warm boundary layer clouds, precipitating clouds are the dominant cloud state in July over the study region, with a total frequency of occurrence of 46% (Fig.2e). The increase in cloud LWP with increasing N_d is observed primarily in heavily precipitating thick clouds with N_d < 30 cm^{-3} and LWP > 125 gm^{-2} (Fig.2a). However, these clouds occur relatively infrequently at ENA, accounting for only 2% of the total warm boundary cloud population (Fig.2e). In contrast, most of the precipitating clouds at ENA are lightly precipitating with $15 < r_e < 20\ \mu m$ (Fig.2e and Fig.S2c) and they exhibit a slight decrease of LWP with N_d (Fig.2a). The mean LWP susceptibility for lightly precipitating clouds ranges from -0.5 to -0.2 for different bins, with a mean value of -0.4. The standard deviations of LWP susceptibility in different LWP-N_d bins vary between 0.4 to 1.2, while the LWP susceptibilities for precipitating clouds are significantly different than other two cloud states at a 95% confidence level. The slight decrease in LWP for lightly precipitating clouds aligns with previous findings over the Pacific, Atlantic, and global oceans for marine stratocumulus (e.g., Fig S4 in Zhang and Feingold, 2023).

12

357   The contrasting response of LWP to N_d perturbations for lightly and heavily precipitating clouds can be

358   attributed to the interplay of two competing processes: the depletion of LWP caused by the sedimentation-

359   evaporation-entrainment feedback and the accumulation of LWP resulting from the precipitation suppression

360   feedback. Heavily precipitating clouds are predominantly overcast with a mean CF of 0.65 (Fig.S2a) and a mean r_e

361   of 25 μm (Fig.S2c). Precipitation acts to stabilize the boundary layer, remove water from cloud top, and reduce the

362   entrainment rate (Sandu et al., 2007, 2008). Therefore, heavily precipitating clouds exhibit smaller entrainment rate

363   than non-precipitating clouds with similar LWP. The increase of LWP from precipitating suppression feedback

364   outweighs the decrease of LWP from entrainment feedback and results in a net increase in LWP (e.g., Chen et al.,

365   2014; Toll et al., 2019). In lightly precipitating clouds, however, the suppression effect of drizzle on the entrainment

366   rate is minimal. Therefore, the decrease in LWP from entrainment overpowers the increases in LWP from

367   precipitating suppression, leading to a net decrease in LWP with increasing N_d (e.g., Xue and Feingold, 2006).

368   Precipitating clouds generally exhibit brighter cloud albedo with increasing N_d as a result of the weak

369   negative and positive LWP adjustment, particularly in heavily precipitating clouds (Fig.2b). For lightly precipitating

370   clouds, α_c susceptibilities range from -0.04 to 0.07 $ln(N_d)^{-1}$, with a mean of 0.02 $ln(N_d)^{-1}$. The suppression of

371   precipitation by N_d also lead to a significant increase in CF for heavily precipitating clouds, with slopes greater than

372   0.25 $ln(N_d)^{-1}$. For most of the lightly precipitating clouds, the mean CF exhibits small variation with N_d

373   perturbations, with CF susceptibilities ranging between ± 0.025 $ln(N_d)^{-1}$ (Fig.2c). The standard deviation of the

374    $1°$ α_c and CF susceptibilities for different precipitating bins ranges between 0.05-0.15 and 0.3-0.6, respectively. The

375   α_c and CF susceptibilities for precipitating clouds are significantly different than other two cloud states at a 95%

376   confidence level. Considering the combined effects of increased α_c and CF, the mean radiative response for

377   precipitating clouds amounts to -13 W $m^{-2}ln(N_d)^{-1}$, which is a cumulative shortwave susceptibility of bins

378   classified as precipitating clouds in Fig.2d, weighted by their frequency of occurrence. The contributions from CF

379   and α_c effects are -9.5 and -3.5 W m^{-2} $ln(N_d)^{-1}$, respectively (Eq. 3).

380   *b.   Non-precipitating thick clouds*

381   Non-precipitating thick clouds are less frequent, the total frequency of occurrence is 10% (Fig.2e). Their

382   cloud LWP responses to N_d perturbations differ from that of precipitating clouds. The LWP susceptibility for non-

383   precipitating thick clouds is the most negative among the three cloud states, and it reaches a minimum value of -1.2

384   at the high-LWP and high-N_d ends (Fig.2a). As LWP and N_d decrease, the LWP susceptibility gradually increases

385   from -1.2 to -0.6. This negative susceptibility is likely explained by the evaporation enhancement associated with

386   smaller droplets at high N_d values (e.g., Xue and Feingold, 2006; Small et al., 2009), which works in concert with an

387   entrainment strengthening expected in clouds with large LWP (e.g., Sandu et al., 2008, Williams and Igel, 2021). In

388   addition, clouds with higher N_d and larger LWP exhibit stronger shortwave absorption, which enhance LWP

389   depletion and therefore a more negative LWP susceptibility (e.g. Bores and Mitchell, 1994; Petters et al. 2012). The

390   mean LWP susceptibility for non-precipitating thick clouds is -0.94. Consistent with the negative LWP

391   susceptibility, non-precipitating thick clouds become less reflective with increasing N_d for all N_d bins with LWP $>$

392   75 gm^{-2} (Fig.2b). The mean α_c susceptibility is -0.04 $ln(N_d)^{-1}$. Due to the enhanced entrainment and

393   evaporation, the mean CF mostly decreases with increasing N_d, with the mean CF susceptibilities ranging from -0.1

13

394 to $+0.04 \ln(N_d)^{-1}$ (Fig.2c). Considering the decrease in both α_c and CF, non-precipitating thick clouds exhibit a

395 warming effect at the surface, the mean radiative response is $+4.4 \, W \, m^{-2} \, \ln(N_d)^{-1}$ (Fig.2d), with contributions

396 from the albedo effect and the CF effect of 2.9 and $1.5 \, W \, m^{-2} \, \ln(N_d)^{-1}$, respectively.

c. Non-precipitating thin clouds

398 Non-precipitating thin clouds are more common than thick clouds during summer, with a total frequency of

399 occurrence of 44% (Fig.2e). Compared to non-precipitating thick clouds, they exhibit consistent negative but

400 slightly weaker LWP responses to N_d perturbations. The mean LWP susceptibilities range from -0.9 to -0.4 in

401 different LWP-N_d bins with a mean of -0.7 (Fig.2a). Similar to non-precipitating thick clouds, non-precipitating

402 thin clouds mostly become darker with increasing N_d. Interestingly, with largely decreased LWP, the mean CF

403 mostly increase for all N_d conditions, the CF susceptibilities range from $+0.02$ to $+0.25 \ln(N_d)^{-1}$ (Fig.2c). The

404 sedimentation- evaporation-entrainment feedback alone cannot explain the opposite signs in in LWP and CF

405 susceptibilities for non-precipitating thin clouds. A possible explanation for the increased CF is that the enhanced

406 cloud top radiative cooling rate from aerosol perturbations help to mix the boundary layer, facilitate moisture

407 transport from the ocean surface to cloud, and therefore favor new cloud formation and extend cloud lifetime (e.g.,

408 Christensen et al. 2020). This hypothesis is consistent with and supported by the relative low CF for these clouds

409 (Fig.S2a) and the diurnal variation in LWP susceptibility for non-precipitating thin clouds, which will be discussed

410 in the next section. The opposite signs of LWP and CF susceptibilities indicate that the AIE might redistribute cloud

411 water horizontally and make the thin clouds thinner and wider. The CF radiative effect from increased CF

412 dominates the albedo effect from darker clouds and lead a net cooling at the surface. The mean radiative response is

413 $-5.2 \, W \, m^{-2} \ln(N_d)^{-1}$, with CF and albedo contributions of -8.3 and $+3.1 \, W \, m^{-2} \ln(N_d)^{-1}$, respectively (Fig.2d).

414 To sum up, the magnitudes and signs of the responses of cloud LWP, α_c, and CF to N_d perturbations

415 primarily depend on the cloud states. Precipitating clouds mostly become thinner and brighter with increasing N_d,

416 accompanied by a slight increase in CF. An increase in LWP with increasing N_d is observed only for heavily

417 precipitating clouds with $N_d < 30 \, cm^{-3}$ and LWP $> 125 \, gm^{-2}$. Non-precipitating thick clouds become thinner, less

418 reflective, and decrease in cloudiness with N_d perturbations. On the other hand, non-precipitating thin clouds

419 become thinner and less reflective, but their cloudiness increase as N_d increases. Given the dependence of AIE on

420 cloud state, we will apply the cloud state classification in the following two sections with the goal of facilitating a

421 process-level understanding of cloud responses and the daytime variation in cloud susceptibilities.

3.3 Daytime variation of cloud susceptibility

423 As discussed in the introduction, warm boundary layer clouds exhibit a distinct diurnal cycle in both cloud

424 properties and frequency of occurrence of cloud states during summer. In this section, we investigate the daytime

425 variation of cloud susceptibility from 9 to 18 local standard time (LST) using the half-hourly Meteosat-11 retrievals.

426 The domain mean daytime variation of cloud susceptibility is estimated from each half-hourly time step within each

427 $1° \times 1°$ box and then averaged over the study domain (33-43°N, 23-33°W) during the four months. In the study

428 domain, there is little spatial variability in cloud susceptibilities and the diurnal cycle of the cloud susceptibility for

429 the $1° \times 1°$ box at the ARM ENA site agree well with the domain mean pattern (not shown). Furthermore, diurnal

14

430 cycle of the cloud microphysical properties (e.g., r_e, τ, LWP, N_d) show little difference between the domain mean

431 value or that averaged over the 1° × 1° box at the ARM ENA site. The cloud microphysics retrievals from

432 Meteosat-11 agree well with retrievals based on ground-based radar and lidar observations in the daytime variation

433 (not shown). Therefore, the ARM ENA site at the Azores archipelago can represent the cloud properties and the AIE

434 for warm boundary layer clouds over the study region.
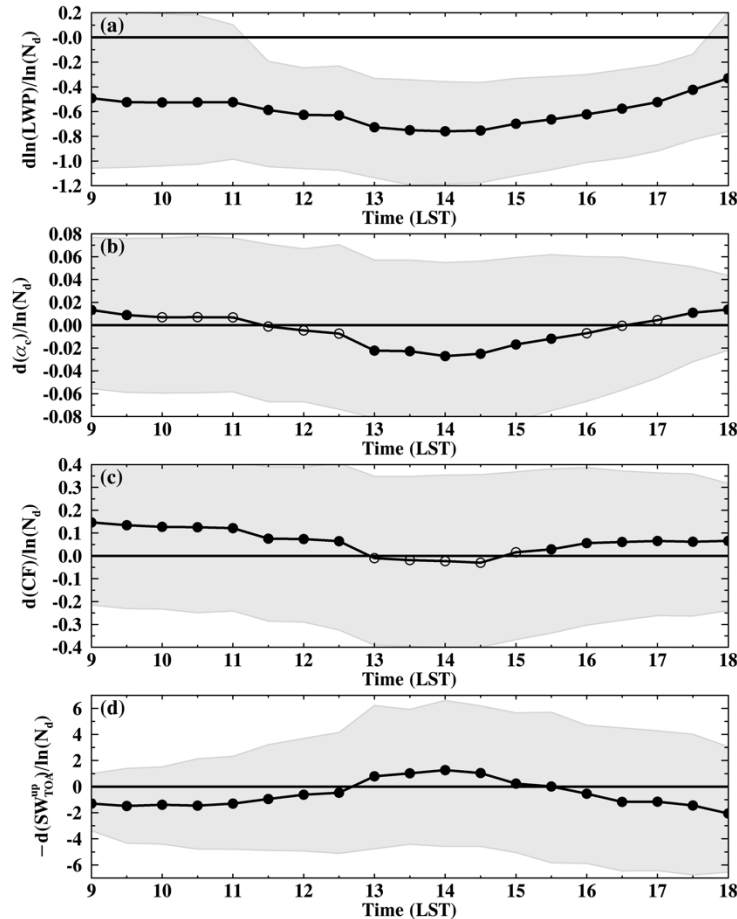
435
436 Figure 3. Daytime variation of cloud susceptibilities. (a) cloud LWP susceptibility ($dln(LWP)/dln(N_d)$), (b) cloud
437 albedo susceptibility ($d\alpha_c/dln(N_d)$), (c) cloud fraction susceptibility ($dCF/dln(N_d)$), and (d) cloud shortwave
438 susceptibility ($-dSW_{TOA}^{up}/dln(N_d)$). The shaded areas represent the lower and upper 25th percentile of the cloud
439 susceptibilities for each time step and the solid lines with dots represent the mean values. In (b) and (c), filled
440 markers indicate data points~~hours~~ that susceptibilities are significantly different from zero (p<0.05), while open
441 markers indicate statistical insignificance.

442

443   Warm boundary layer clouds witness distinct and significant daytime variations in cloud susceptibilities

444 (Fig.3). For example, the mean LWP susceptibility exhibits a magnitude of change of 0.4 from morning to evening,

445 which corresponds to approximately 30-40% of the overall variability in LWP susceptibility (Fig.3a). Similarly, the

446 α_c and CF susceptibility undergo magnitude of changes of approximately 20-30% compared to the overall

447 variability (Figs. 3b and c). The high variability in cloud susceptibility highlights the complex synoptic,

448 meteorological and cloud conditions as well as the interplay between them in the ENA region. Nevertheless, the

15

449 daytime variation of cloud susceptibility is statistically significant at a 95% confidence level based on a student's t-

450 test. Interestingly, all three cloud variables exhibit a "U-shaped" diurnal cycle in cloud susceptibilities with less

451 negative/more positive values in the morning and evening and more negative values at noon. Additionally, both the

452 α_c and CF susceptibilities switch signs from positive in the morning to negative at noon, and then become positive

453 again in the evening. The switch in sign for albedo susceptibility is statistically significant at a 95% confidence

454 level, while the switch in sign for CF susceptibility is not statistically significant (Figs. 3b, c). As both α_c and CF

455 increase with increasing N_d in the morning, AIE has a cooling effect at the surface and the estimated shortwave

456 susceptibility is $-1.4\ W\ m^{-2}\ ln(N_d)^{-1}$. During 13-15 LST, the shortwave susceptibility switches sign to a warming

457 effect of $+1.2\ W\ m^{-2}\ ln(N_d)^{-1}$ (Fig.3d).

458   Given the pronounced daytime variation of cloud susceptibility, *how can we explain this distinct daytime*

459 *variation, and which state of cloud contributes most to the daytime variation?* One possible explanation is the

460 increased occurrence of precipitating clouds in the morning and evening during summer (Remillard et al, 2012),

461 which increase cloud susceptibility, as depicted in Fig.2. To investigate this hypothesis and quantify the impacts of

462 different cloud states on the variabilities of cloud susceptibilities, we examined the daytime variation of cloud

463 susceptibility, along with the daytime shift in occurrence frequency for each cloud state.

464 **3.4 Daytime variation of cloud susceptibility for different cloud states**

465 **3.4.1 Non-precipitating thin clouds**

466   Non-precipitating clouds mainly consist of thin clouds, with a daytime mean occurrence of 44% (Fig.4a).

467 The highest occurrence is observed around noon, which is consistent with ground-based radar reflectivity

468 measurement at the ENA site (Remillard et al, 2012). Furthermore, as seen in Fig.4, not only the frequency of cloud

469 occurrence, but also the susceptibilities of LWP, α_c, and CF show distinct daytime fluctuations. For example, the

470 mean LWP susceptibility decreases from -0.4 to -0.9, and the mean α_c susceptibility decreases from 0.02 to -0.04

471 $ln(N_d)^{-1}$ from morning to noon, followed by increases in both LWP and α_c susceptibilities in the afternoon. The

472 CF susceptibility is highly positive in the morning and decreases to near zero after 13 LST. In addition, cloud

473 susceptibility for thin clouds in the morning is statistically significantly different from that at noon and in the

474 evening at a 95% confidence level.

475

16
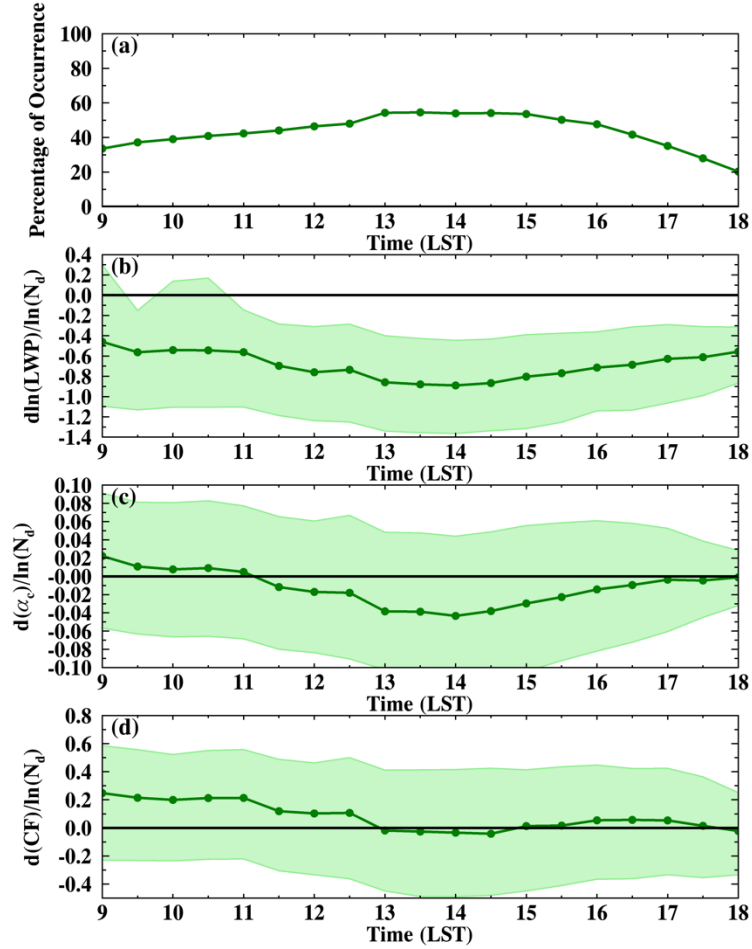
Figure 4. Daytime variation of (a) percentage of occurrence of non-precipitating thin clouds to warm boundary layer clouds, (b) cloud LWP susceptibility ($dln(LWP)/dln(N_d)$), (c) cloud albedo susceptibility ($d\alpha_c/dln(N_d)$), and (d) cloud fraction susceptibility ($dCF/dln(N_d)$) for non-precipitating thin clouds. The shaded areas represent the lower and upper 25th percentile of the cloud susceptibilities for each time step and the solid lines with dots represent the mean values.

To explain the decrease of cloud susceptibility of non-precipitating thin clouds from morning to noon, we test two hypotheses (H1 and H2 in Table 1). Hypothesis H2 is related to the dissipation of thin clouds during this period, which is caused by a decreased LWP due to increased solar radiation. During the dissipation, both LWP and r_e decrease. As r_e is raised to the power of $-\frac{5}{2}$ in Eq. (1) compared to τ being raised only to the power of $\frac{1}{2}$, the decreases of LWP and r_e could still result in an increase in the retrieved N_d. Consequently, a LWP decrease and N_d increase lead to a decrease in LWP susceptibility during the dissipation (Gryspeerdt et al., 2019). To examine this hypothesis (H2), non-precipitating thin clouds are classified as: growing, dissipating, or constant based on the changes in the mean CF, cloud susceptibilities for the three groups are shown in Fig.S3. More specifically, we calculate the change in the mean CF within a 30-minute window for each fixed $1° \times 1°$ box. If the mean CF increase (decrease) more than 10%, clouds are classified as growing (dissipating). If the change in CF is less than 10%, clouds are classified as constant. Similar results are obtained using classification methods based on different CF thresholds (e.g., from 10% to 30%), and during different time windows from 30-minutes to two hours (not shown).

Table 1. List of hypotheses and associated explanations for the daytime variation of LWP and CF susceptibilities for different cloud states.

	Cloud state	Hypotheses:	
Daytime evolution of LWP susceptibility	Non-precipitating thin clouds	H1*:	Non-precipitating thick clouds transition to thin clouds from morning to noon, which leads to a daily minimum LWP susceptibility at noon.
		H2*:	Cannot explain. Clouds that are growing or dissipating have similar LWP susceptibilities as clouds with constant CF.
	Non-precipitating thick clouds	H1:	Thin clouds develop to thick clouds from noon to evening, which leads to an increase in LWP susceptibility.
		H2:	Cannot explain.
	Precipitating clouds	H1:	Non-precipitating thin clouds transition to precipitating clouds in the afternoon, which leads to a decrease in LWP susceptibility.
		H2:	Cannot explain.
Daytime evolution of CF susceptibility	Non-precipitating thin clouds	H1:	Thick clouds transitioned to thin clouds from morning to noon, leading to a decrease in CF susceptibility
		H2:	Cannot explain.
	Non-precipitating thick clouds	H1:	Cannot explain.
		H2:	Cannot explain.
		H3*:	Mostly overcast clouds in the morning and evening. CF of overcast clouds is less sensitive to N_d perturbations.
	Precipitating clouds	H1:	Thin clouds transition to precipitating clouds in the afternoon, and lead to a decrease in CF susceptibility
		H2:	Cannot explain.

*H1: LWP and CF responses to N_d perturbations slower than the transition of cloud state.
*H2: Dissipation or development of clouds.
*H3: Changes in cloud morphology.

As seen in Fig. S3b, the LWP susceptibilities for non-precipitating thin clouds in the growing or dissipating stages are similar or less negative than clouds that remain constant in CF, which contradicts the hypothesis H2. Additionally, the occurrence of dissipating and developing thin clouds remain relatively constant throughout the day (Fig.S3a), which differs from our hypothesis that thin clouds dissipate in the morning. Therefore, the decrease in LWP susceptibility in the morning is *unlikely* to be attributed to the dissipation or development of thin clouds. Yet, due to the observational limitation on estimating the mixing process from satellite retrievals, further investigation is needed to quantify the impact of cloud dissipation on the N_d-LWP relationship.

Besides the change in CF, dissipation/development of clouds can be defined by change in LWP. However, as our definition of thin and thick clouds use LWP thresholds, results based on change in LWP are similar to results shown in Fig.5, but with weaker signal (not shown). This indicates that classification of precipitating versues non-precipitating clouds is necessary in distinguishing cloud responses to N_d perturbations rather than merely using the LWP threshold.

18

511   Hypothesis H1 is related to the response time of cloud LWP and CF to N_d perturbations. Both numerical

512   models and observations have shown that the influence of aerosols on cloud LWP, achieved through adjusting the

513   entrainment rate, may take four hours to become apparent and up to 20 hours to reach an equilibrium (e.g.,

514   Glassmeier et al. 2021; Gryspeerdt et al., 2021; Fons et al., 2023). Similarly, CF increases gradually from increasing

515   aerosols and may take approximately three to four hours to reach its maximum effect after the initial perturbation

516   (Gryspeerdt et al., 2021). Therefore, we hypothesize that if clouds change state during the adjustment time, clouds

517   may still retain the "memory" of their ~~susceptibilities~~ responses to N_d perturbations from the previous state. The

518   possible physical processes and mechanisms for this hypothesis is that the LWP susceptibility is mainly driven by

519   cloud top evaporation and entrainment rate. The positive feedback among entrainment, evaporative cooling, long-

520   wave radiative cooling, and mixing from cloud top form a positive feedback loop and set up an environment

521   conductive to enhanced entrainment and evaporation. These feedback and environment will not change immediately

522   even when the cloud LWP decrease and cloud transition to a thin state or vice versa. With the diurnal variation in

523   cloud properties and transition in cloud state, it leads to a diurnal evolution in cloud susceptibility.

524   To quantify the dependence of current cloud susceptibility on previous cloud states, we track the cloud state

525   for each 1° × 1° box backward in time for two hours and classify the non-precipitating thin clouds into three groups

526   (Fig.5): (1) thin clouds that are currently classified as thin clouds and didn't change states in the past two hours (thin

527   → thin), (2) thin clouds that evolved from precipitating clouds (rain → thin), and (3) thin clouds that decayed from

528   non-precipitating thick clouds (thick → thin). This backward tracking classification is applied at each time step. As

529   shown in Fig.5a, at 9 LST, ~50% of the non-precipitating thin clouds originate from thick clouds in previous hours.

530   The transition from thick to thin clouds is likely caused by the increased solar radiation after sunrise, leading to

531   cloud turbulent decoupling from the ocean surface and a decrease in cloud LWP. In the evening, on the other hand,

532   around 80% of the thin clouds are thin clouds in previous hours. In addition, less than 20% of the non-precipitating

533   thin clouds transition from precipitating clouds.

534   In consistent with our hypothesis, non-precipitating thin clouds that are previously thick have significantly

535   more negative LWP and α_c susceptibilities than thin clouds that are previously thin or precipitating (Figs. 5b and c).

536   The differences between the two categories are most pronounced from late morning to early afternoon and less

537   pronounced in the early morning and evening. Such pattern is likely attributed to the daytime evolution of marine

538   boundary layer and cloud coupling state. For example, in the early morning (e.g., 9-10 LST), even with higher

539   frequency of occurrence of thick clouds transitioning to thin clouds, the LWP susceptibility for the thick-to-thin

540   category is less negative compared to later time (dashed line with diamond symbols in Figs 5a, b). This is attributed

541   to the less negative LWP susceptibility for non-precipitating thick clouds in earlier time (e.g., 7-9 LST, not shown),

542   in connection with a well-mixed boundary layer able to transport moisture from the ocean to the cloud, which

543   compensates the moisture loss from aerosol-enhanced entrainment (e.g., Sandu et al., 2008), so that both thick and

544   thin clouds exhibit less negative LWP susceptibilities. From late morning to early afternoon, with increasing solar

545   radiation, deepening of boundary layer and clouds decoupled from surface, LWP susceptibility for thick clouds

546   largely decreases and reaches a daily minimum, which contributes to the largest difference between the thin-to-thin

547   and thick-to-thin categories shown in Fig.5b. The opposite processes occur f~~F~~rom afternoon to evening, LWP of

19

550 our hypothesis that clouds retain the memory of their responses to N_d perturbations from their previous states.
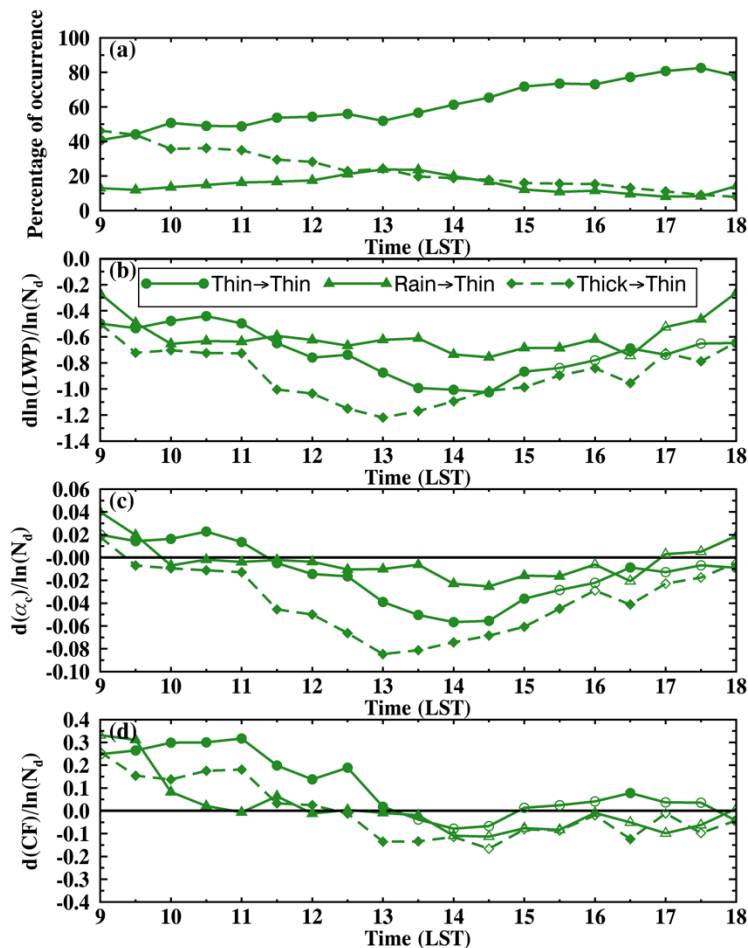
551
552 Figure 5. Daytime variation of non-precipitating thin clouds transition from non-precipitating thin clouds (thin →
553 thin, solid line with circle symbols), precipitating clouds (rain → thin, solid line with triangle symbols), and non-
554 precipitating thick clouds (thick → thin, dashed line with diamond symbols) in previous two hours. Symbols for
555 different state transitions are noted in (b). In (b)-(d), filled markers indicate data points that are significantly
556 different from the other two groups (p<0.05), while open markers indicate statistical insignificance.

557   Similar to LWP, responses of CF to N_d perturbations in the morning retain the memory of the previous

558 state of clouds. As seen in Figure 5d, thin clouds that transitioned from thick clouds or precipitating clouds have

559 significantly less positive CF susceptibility than thin clouds that were previously thin, particularly in the morning.

560 As the CF susceptibility for thin clouds that evolved from precipitating and thick clouds greatly decrease from

561 morning to noon, the CF susceptibility for thin clouds decrease from large positive to near zero from morning to

562 noon (Fig.4c). A maximum in CF susceptibility in the early morning is likely associated with the influence of

563 aerosols on boundary layer mixing and the evolution of boundary layer from morning to noon. The enhanced

564 entrainment rate and radiative cooling rate from N_d perturbations help to destabilize the boundary layer and

565 transport moisture from the ocean surface to clouds, facilitating new cloud formation (e.g., Christensen et al. 2020).

566 As the boundary layer is typically well mixed in the morning with clouds coupled to the surface, the impact of

567   aerosols on CF is strongest in the morning and gradually decrease from morning to noon. In the afternoon, thin

568   clouds transition from all three states have near-zero CF responses to N_d perturbations. Further analyses and model

569   simulations are needed to better understand the impacts of aerosols' impact and the associated diurnal evolution of

570   entrainment rate, boundary layer mixing on, cloud cover and lifetime, to better explain the observed daytime

571   variation of CF susceptibility for non-precipitating thin clouds.

572   Lastly, Thethe impact of the cloud memory of AIE on current cloud susceptibility is also evident within a

573   30-minute window when a transition of cloud state just occurs (Fig.S4). Consistent with the findings in Fig.5, thin

574   clouds that transition from thick clouds exhibit much more negative LWP and α_c susceptibilities compared to thin

575   clouds that remain thin during the 30 minutes. Yet, the number of cases experiencing a transition in cloud state

576   within a 30-miniute window is limited (Fig.S4a). In addition, the impact of the transition in cloud state on the

577   current cloud susceptibility persists for at least four hours (Fig.S5). As our tracking method does not follow

578   individual cloud parcels to track changes in their states, the influence of cloud advection may become significant

579   over longer tracking time, such as four hours. Therefore, a two-hour tracking window is used in this study.

580   As discussed in the method section, while the advective effects in our study are expected to be modest, we

581   further isolate their impact, by performing an analysis for cloud scenes with wind speed of less than 7 m/s (60% of

582   time), when clouds are somewhat stationary in two hours. Influence of transition in cloud state is consistent as in

583   Fig.5 with more negative LWP and α_c susceptibilities for thin clouds transitioned from thick clouds, while the signal

584   is slightly stronger (not shown). This consistency confirms that our tracking method can capture the signal of cloud

585   state transition and its impact on cloud susceptibilities during summer in the study region.

586   In summary, the "U-shaped" daytime variations in LWP and α_c susceptibilities for non-precipitating thin

587   clouds are likely due to cloud retaining the memory of AIE. From morning to noon, as non-precipitating thick

588   clouds evolve to thin clouds, they retain their memory of the large negative LWP susceptibility. Therefore, both

589   LWP and α_c susceptibilities decrease from morning to noon for thin clouds and reach their daily minima at noon. In

590   the afternoon, as a growing percentage of thin clouds persist as thin clouds during the next hours, LWP and α_c

591   susceptibilities gradually increase to less negative and near zero, respectively.

3.4.2 Non-precipitating thick clouds
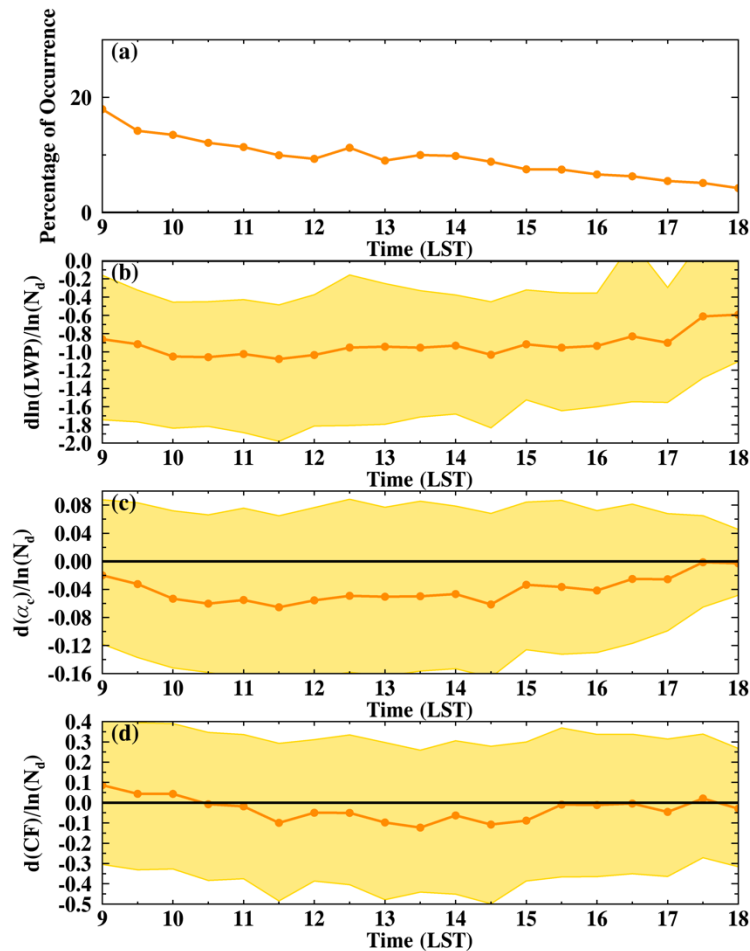
Figure 6. Daytime variation of (a) percentage of occurrence of non-precipitating thick clouds to warm boundary layer clouds, (b) cloud LWP susceptibility ($dln(LWP)/dln(N_d)$), (c) cloud albedo susceptibility ($d\alpha_c/dln(N_d)$), and (d) cloud fraction susceptibility ($dCF/dln(N_d)$) for non-precipitating thick clouds. The shaded areas represent the lower and upper 25th percentile of the cloud susceptibilities for each time step and the solid lines with dots represent the mean values.

Consistent with Fig.2e, non-precipitating thick clouds are the least frequent warm boundary layer cloud state during summer over the ENA region. Their percentage of occurrence continuously decreases from 20% in the morning to less than 5% in the evening (Fig.6a). For LWP and α_c, their susceptibilities first decrease from less negative to more negative in the morning and then increase from noon to evening (Fig.6b and c, respectively). CF susceptibility is weakly positive in the early morning, becomes weakly negative from late morning to early afternoon, and increases to near zero in the evening (Fig.6d). The daytime evolutions of LWP and α_c susceptibilities for thick clouds exhibit consistent trend with cloud susceptibilities for thin clouds transition from thick clouds shown in Fig.5 but with a lag of two hours. For example, the LWP susceptibility for thick clouds decreases from -0.8 to -1.1 from 9 to 11 LST and it increase from -1.1 to -0.8 from 11 to 16 LST; while the LWP susceptibility for the thick-to-thin category in Fig.5b decreases from -0.8 to -1.2 from 11-13 LST and increases to -0.6 from 13 to 18 LST. This result supports our hypothesis on cloud retaining its memory of AIE of its previous cloud state.

22

To gain insight into the observed evolution of LWP and α_c susceptibility from morning to evening, we investigate the influence of cloud state transition on cloud susceptibility for non-precipitating thick clouds, which is summarized as H1 in Table 1. As shown in Fig.7a, around 40% of thick clouds sustain as thick clouds from the previous two hours in the morning; whereases during the late afternoon to evening, with decreasing solar radiation, more than 60% of thick clouds are developed from thin clouds. Consistent with the findings presented in Fig.5, thick clouds that are previously thick exhibit significantly more negative LWP susceptibility compared to thick clouds that are previously thin (Fig.7b). These differences are particularly prominent from late morning to noon and become insignificant in the afternoon. As discussed before, difference between the thick-to-thick and the thin-to-thick categories are due to the LWP susceptibilities for thick and thin clouds of previous time, while the smaller differences in the early morning and afternoon could be attributed to the expected stronger turbulence and cloud coupling at these times. Additionally, Fig.7d indicates that transition in cloud state cannot explain the daytime variation in CF susceptibility for thick clouds, as all three groups are insignificantly different from each other.
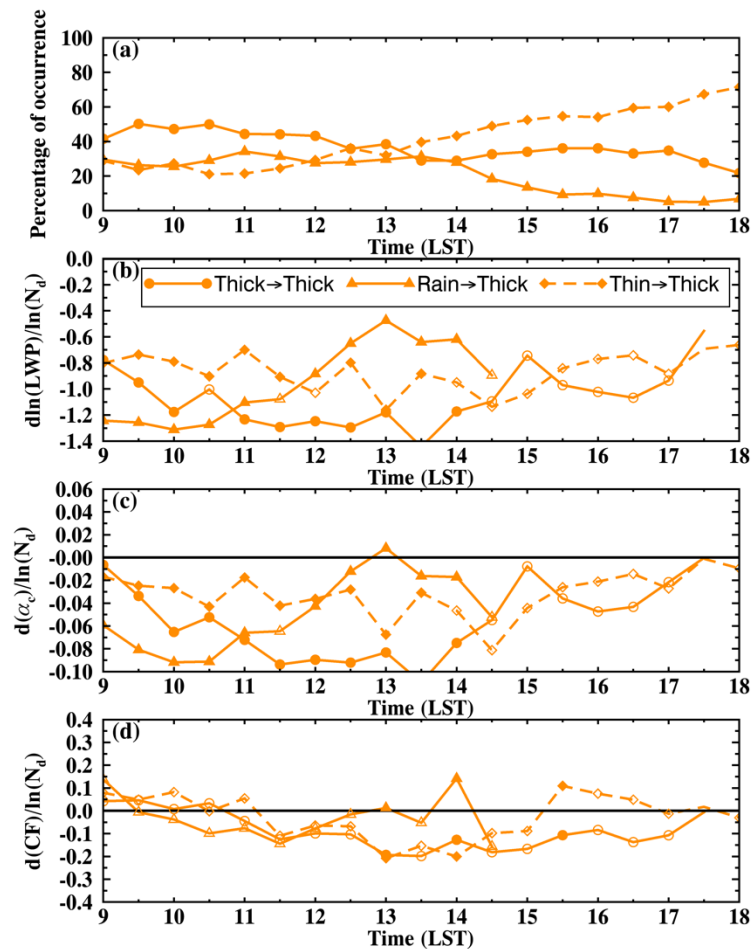
Figure 7. Daytime variation of non-precipitating thick clouds transition from non-precipitating thick clouds (thick → thick, solid line with circle symbols), precipitating clouds (rain → thick, solid line with triangle symbols), and non-precipitating thin clouds (thin → thick, dash line with diamond symbols) in previous two hours. Symbols for different state transitions are noted in (b). In (b)-(d), filled markers indicate data points that are significantly different from the other two groups (p<0.05), while open markers indicate statistical insignificance.

628   To understand the driving mechanism for the daytime variation in CF susceptibility shown in Figure 6d, we
629 calculate the mean cloud properties for non-precipitating thin and thick clouds, as shown in Fig.8. In the morning,
630 non-precipitating thick clouds are predominantly overcast clouds with a mean CF of 75% (Fig.8a). To distinguish
631 between overcast and broken clouds, we calculate the diameter-to-height ratio (DHR) for each cloud, where
632 diameter is estimated by the square root of the area and height is defined as the 90th percentile of cloud tops. As
633 shown in Fig.8c, thick clouds are mostly overcast in the morning with a mean DHR of 230. Compared to broken
634 clouds, overcast clouds have less room for CF to increase, which results in a less positive CF susceptibility for thick
635 clouds compare to thin. After 10 am, non-precipitating thick clouds start to break. The mean CF decreases from 75%
636 at 10 am to 60% at 2 pm and the DHR decreases from 230 to 170. As CF for broken clouds is more sensitive to N_d
637 perturbations, CF susceptibility decreases to $-0.13\ ln(N_d)^{-1}$, which is consistent with the daytime mean negative
638 CF susceptibility shown in Fig.2c. From afternoon to evening, clouds transition to overcast again (Fig.8), and the CF
639 susceptibility increases back to zero. This impact of cloud morphology (e.g., overcast or broken clouds) on daytime
640 variation of CF susceptibility is summarized as H3 in Table 1.
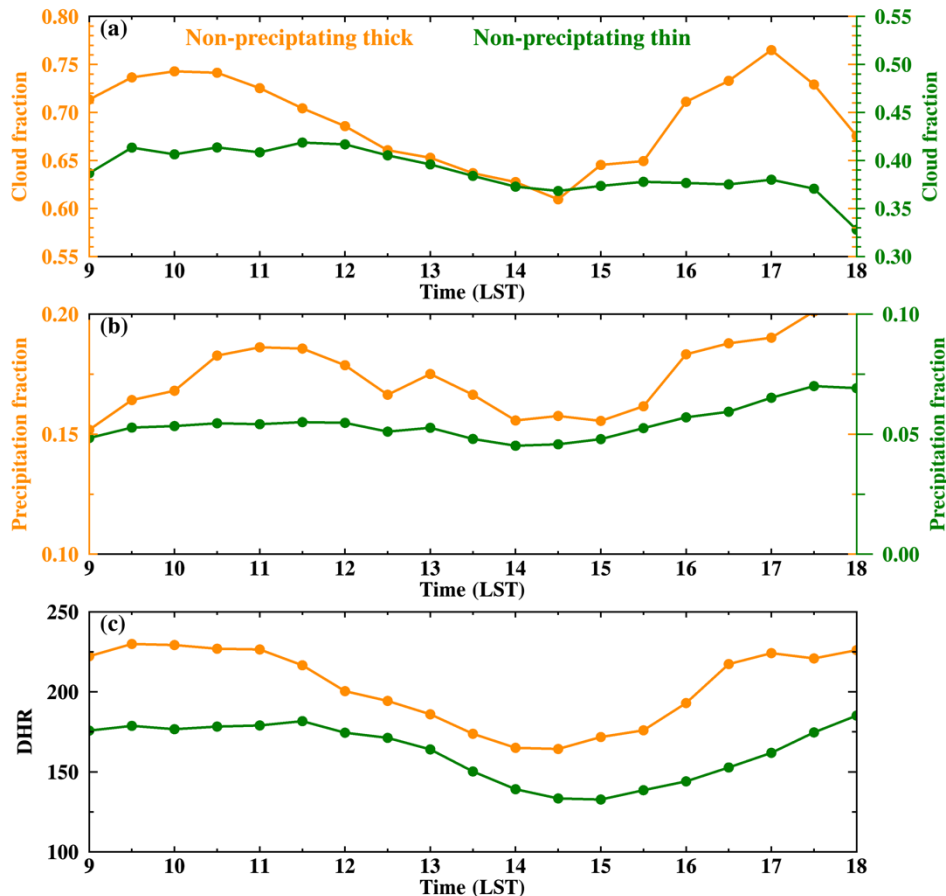
641
642   Figure 8. Diurnal variation of (a) cloud fraction, (b) pixel-level precipitation fraction, and (c) diameter-to-height
643 ratio (DHR) for non-precipitating clouds. Different colors represent different cloud states as indicated in (a). Please
644 note that the non-precipitating thin cloud in (a) and (b) use the y-axis on the right side.

24

645   The previous results are summarized as follows: LWP susceptibility for non-precipitating thick clouds first

646   decreases from less negative to more negative in the morning and then increase from noon to evening, which is

647   likely attributed to the transition from thin to thick clouds. In the morning, 40% to 50% of thick clouds are

648   previously thick clouds, these clouds exhibit a large negative LWP susceptibility. In the afternoon, with increasing

649   percentage of thick clouds develop from thin clouds and retain the memory of LWP ~~susceptibility~~ responses to N_d

650   perturbations of the thin clouds. LWP susceptibility gradually increases and becomes similar to that of thin clouds

651   (Fig.4b, 6b). Daytime variation in CF susceptibility for thick clouds is likely attributed to changes in cloud

652   morphology. In the morning and evening, thick clouds are mostly overcast with CF less sensitive to N_d

653   perturbations, resulting in a near zero CF susceptibility. From late morning to early afternoon, the overcast thick

654   clouds break down and CF decrease with increasing N_d likely due to the increased shortwave absorption, the

655   enhanced entrainment, and evaporation.

656   The impact of cloud memory and transition of cloud state on the daytime variation of LWP susceptibility is

657   summarized as a schematic figure shown in Fig.9. From morning to noon, as non-precipitating thick clouds

658   transition to thin clouds, thin clouds retain their memory of AIE ~~the large negative LWP susceptibility~~ of their

659   previous state. Therefore, LWP susceptibility for thin clouds decreases from morning to noon and reach its daily

660   minima in the early afternoon. From early afternoon to evening, with non-precipitating thin clouds developing to

661   thick clouds, LWP susceptibility for thick clouds increase.
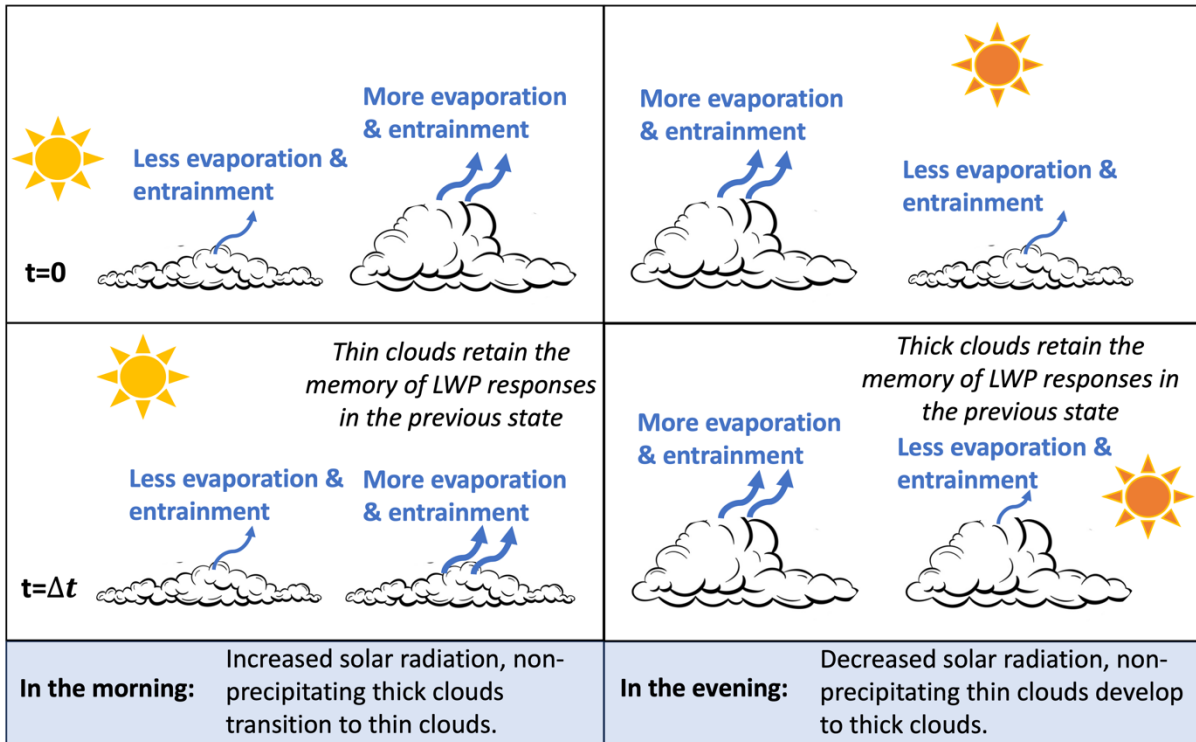
662
663 Figure 9. Schematic figure of influence of cloud memory and transition of cloud state on the LWP susceptibility and
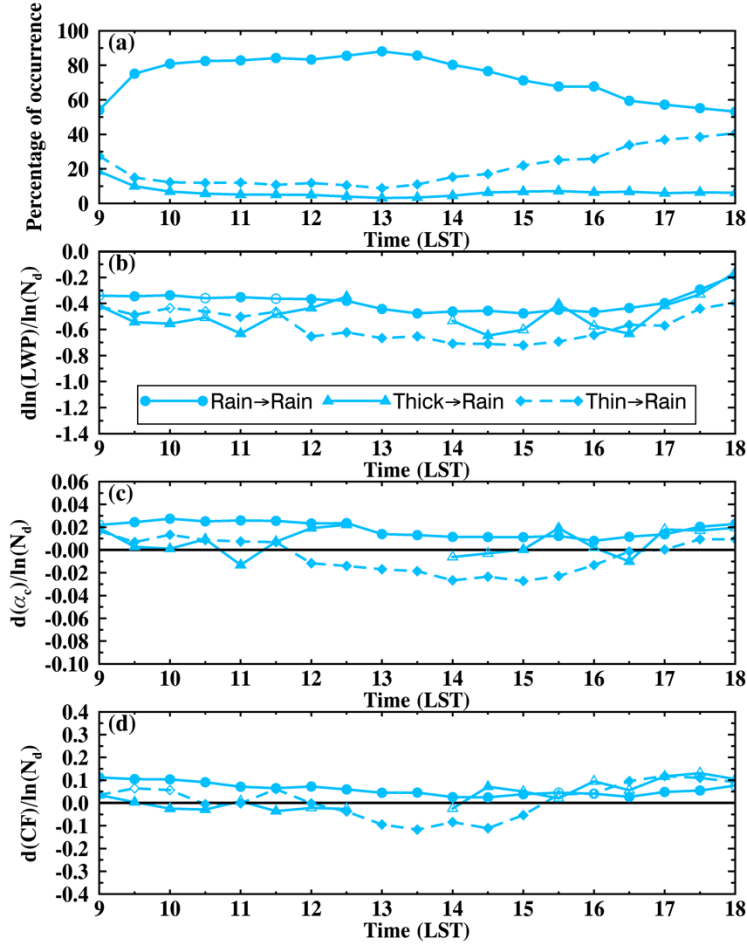664 its daytime variation.

3.4.3 Precipitating clouds
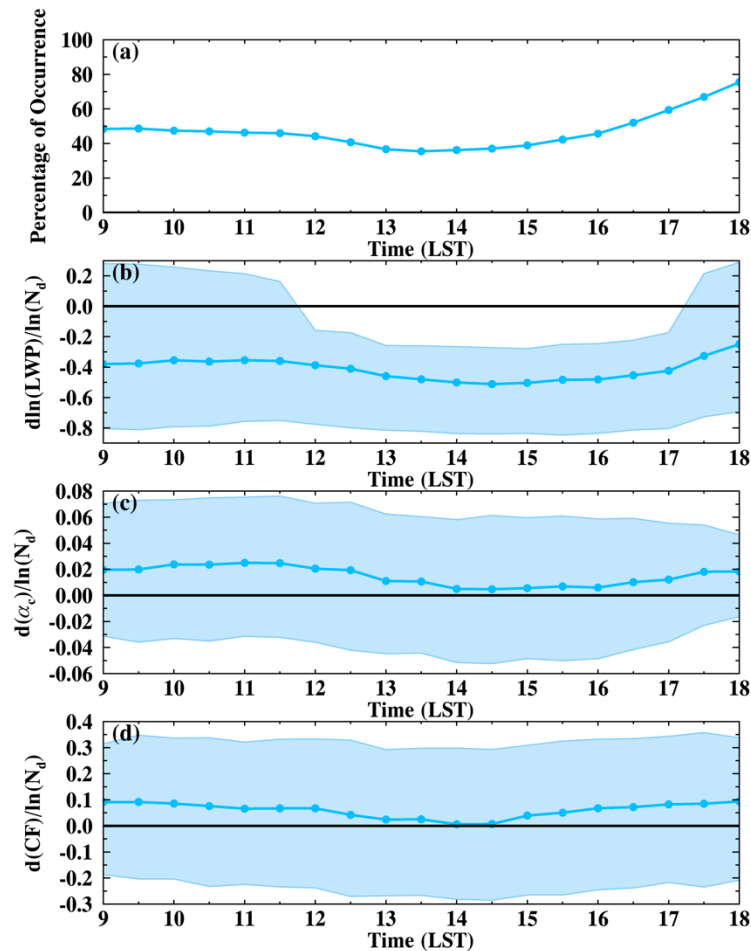
Figure 10. Daytime variation of (a) percentage of occurrence of precipitating clouds to warm boundary layer clouds, (b) cloud LWP susceptibility ($dln(LWP)/dln(N_d)$), (c) cloud albedo susceptibility ($d\alpha_c/dln(N_d)$), and (d) cloud fraction susceptibility ($dCF/dln(N_d)$) for precipitating clouds. The shaded areas represent the lower and upper 25th percentile of the cloud susceptibilities for each time step.

Precipitating clouds, depicted in Figs.10a, are the dominant cloud state in this region, accounting for 46% of the warm boundary layer clouds, compared to 44% of non-precipitating thin clouds. The frequency of precipitating clouds is higher in the morning and evening compared to noon. Throughout the day, the mean LWP susceptibility remain consistently negative, fluctuating between −0.5 to −0.3, with minimum values between 14–16 LST (Figs.10b). The daytime variability in LWP susceptibility for precipitating clouds is much lower than that for non-precipitating thin (e.g., from −0.9 to −0.4) and thick (e.g., from −1.1 to −0.6) clouds. The negative LWP susceptibility is likely due to the prevalence of lightly precipitating clouds, with a mean precipitating fraction ranging from 0.2 to 0.5 (Fig.S2d). The influence of precipitation suppression is smaller than that of the entrainment enhancement. Similarly, α_c susceptibility fluctuates between 0 to 0.02 throughout the day, with near zero α_c susceptibility in early afternoon (Figs.10c). Despite the minimal daytime variation, the LWP and α_c susceptibilities at 13-16 LST are statistically significant different from cloud susceptibilities in the morning and evening at 95%

682 confidence level with the two-tailed t-test. The CF susceptibility for precipitating clouds also shows minimal

683 daytime variation compared to non-precipitating clouds, with a mean value ranging from 0 to 0.1 (Figs.10d).

684   Consistent with non-precipitating clouds, the daytime variation of LWP and α_c susceptibilities for

685 precipitating clouds can be attributed to the transition of cloud states. For example, as shown in Figs.11b-d,

686 precipitating clouds that transition from non-precipitating thin clouds exhibit significantly more negative/less

687 positive cloud susceptibilities than precipitating clouds that are previously precipitating. Meanwhile, α_c and CF

688 susceptibilities switch signs from positive to negative in the afternoon for precipitating clouds transition from non-

689 precipitating thin clouds compared to that are previously precipitating (dash line with diamond symbols in Figs. 11c,

690 d). Starting from 13 LST, when non-precipitating thin clouds transition to precipitating clouds (Fig.11a), LWP and

691 α_c susceptibilities begin to decrease and reach their daily minimum in the late afternoon. Interestingly, as non-

692 precipitating clouds transition to precipitating clouds (Figs.11b and c, thin → rain, thick → rain), their LWP and α_c

693 susceptibilities exhibit both less negative values and smaller daytime variations compared to thin/thick clouds that

694 remain as thin/thick (Figs. 5b and c, thin → thin, Figs. 7b and c, thick → thick). The underlying reason for this

695 observation is currently unclear and warrants further investigation on the sensitivity of AIE for clouds experiencing

696 transition in cloud states, especially between precipitating and non-precipitating clouds. Lastly, the percentage of

697 precipitating clouds that transition from non-precipitating thick clouds is less than 7% (Fig.11a).

698   In conclusion, precipitating clouds exhibit smaller daytime variation in cloud susceptibilities compared to

699 non-precipitating thin and thick clouds. The decrease of LWP and α_c susceptibilities for precipitating clouds in the

700 afternoon is likely contributed by the transition of non-precipitating thin clouds to precipitating clouds.

Figure 11. Daytime variation of precipitating clouds transitioned from precipitating clouds (rain → rain, solid line with circle symbols), non-precipitating thick clouds (thick → rain, solid line with triangle symbols), and non-precipitating thin clouds (thin → rain, dash line with diamond symbols) in previous two hours. Symbols for different state transitions are noted in (b). In (b)-(d), filled markers indicate data points that are significantly different from the other two groups (p<0.05), while open markers indicate statistical insignificance.

Combining the results shown here and results in section 3.4.1, we can answer which cloud state contributes the most to the daytime variation of cloud susceptibility. The non-precipitating thin clouds exhibit similar daytime variations in LWP, α_c, and CF susceptibility than the warm boundary layer clouds (Fig.4 vs. Fig.3), with clouds being less susceptible to N_d perturbations in the morning and evening and more susceptible at noon. Additionally, non-precipitating thin clouds have highest frequency at noon. On the other hand, precipitating clouds, despite their higher percentage of occurrence than thin clouds, exhibit minimal daytime variation in cloud susceptibility. Therefore, the pronounced daytime variations in cloud susceptibilities for warm boundary layer clouds primarily stem from non-precipitating thin clouds. The distinct daytime evolution patterns for the three clouds states highlight the importance of cloud state classification in quantification of cloud susceptibility.

3.5 Contribution to the daytime variation of cloud susceptibility

As discussed in the previous section, both the frequency of occurrence of cloud states and the intensity of cloud responses to N_d perturbations exhibit pronounced daytime variations. In this section, we aim to compare the

28

719　　contribution of these two components to the overall daytime variation in cloud susceptibilities by fixing one

720　　component constant at a time. The contribution from changes in the frequency of cloud states is represented by the

721　　red lines in Fig.12, which is estimated by weighting the daytime mean cloud susceptibility (Figs. 2a-c) with the half-

722　　hourly frequency of occurrence of clouds in the LWP-N_d parameter space, assuming a constant intensity of cloud

723　　susceptibility during the daytime. The contribution from changes in the intensity of cloud susceptibility is depicted

724　　by the blue lines, which is estimated by weighting the half-hourly cloud susceptibility in the LWP-N_d parameter

725　　space with the daytime mean frequency of occurrence of clouds (Fig.2e), assuming a constant frequency during the

726　　daytime. The black line in Fig.12 represents the observed susceptibility shown in Fig.3, and it includes the

727　　contributions from daytime variations in both components.
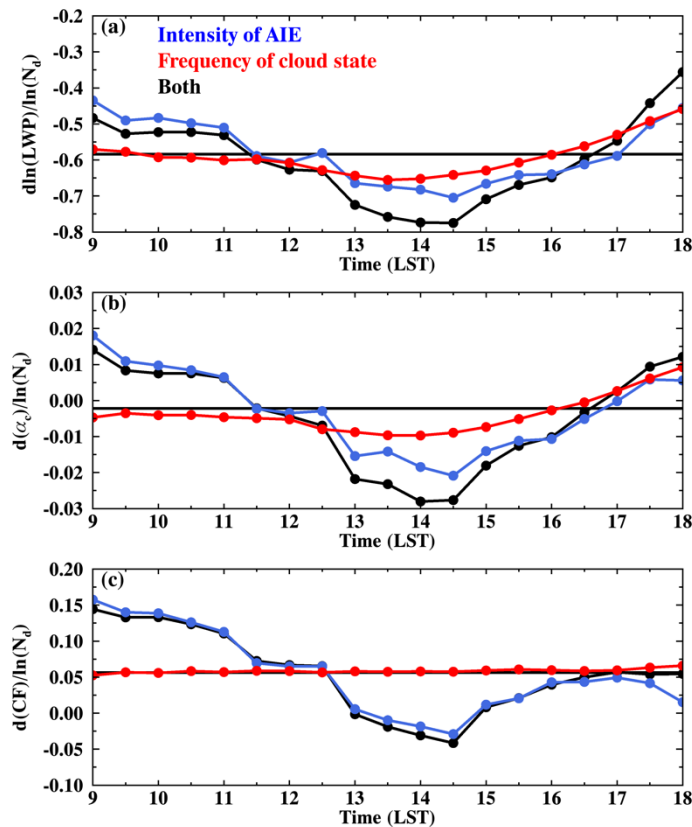
728
729　Figure 12. Daytime variation in cloud susceptibility contributed from the variability in the intensity of susceptibility
730　(blue lines with symbols), variability in the frequency of occurrence of cloud state (red lines with symbols), and
731　from both (black lines with symbols). (a) cloud LWP susceptibility ($dln(LWP)/dln(N_d)$), (b) cloud albedo
732　susceptibility ($d\alpha_c/dln(N_d)$), (c) cloud fraction susceptibility ($dCF/dln(N_d)$). The horizontal black solid lines in
733　(a)-(c) are the daytime mean susceptibility.

734　　　　When comparing the net observed daytime variation of cloud susceptibilities (black lines) with the

735　　contributions from changes in the intensity and the frequency of cloud state (blue and red lines, respectively), we

736　　find that the daytime changes in cloud susceptibility is primarily driven by changes in the intensity of cloud

737　　susceptibilities during the day. Additionally, as shown in Figs. 12a and b, the red lines are close to the daytime mean

738　　values in the morning, which indicates that variations in the frequency of different cloud states have minimal impact

739　　on changes in LWP and α_c susceptibilities in the morning. On the other hand, in the afternoon, both shifts in cloud

740 states and changes in intensities contribute to the changes in LWP and α_c susceptibilities. Compared with LWP and

741 α_c susceptibilities, the daytime variation of CF susceptibility shows minimal sensitivity to changes in cloud state

742 frequency. This limited impact stems from the fact that the daytime fluctuation in cloud state frequency is

743 predominantly influenced by precipitating and non-precipitating thin clouds. Meanwhile, the daytime mean CF

744 susceptibilities for precipitating and non-precipitating thin clouds closely align, measuring at 0.08 and 0.09,

745 respectively (Fig.2c). This convergence diminishes the influence of alterations in the frequency of these two cloud

746 states.

747   In summary, the daytime variation of cloud susceptibility is largely driven by the variation in its intensity.

748 Since polar-orbiting satellites only observe the cloud responses to N_d perturbations across different cloud states at

749 their overpass time, they cannot fully capture the diurnal variation of cloud susceptibilities driven by the variation in

750 the intensity of cloud susceptibility. Given that all three cloud susceptibilities reach their daily minimum at around

751 13:30 LST, studies based on polar-orbiting satellite with overpass time at noon may underestimate the daily mean

752 value of cloud susceptibility.

753 **4. Discussions**

754   In this study, we quantify the susceptibility of warm boundary layer clouds to N_d perturbation using the

755 pixel-level SEVIRI cloud retrievals of each time step. For heavily precipitating clouds, LWP increases under pristine

756 condition (e.g., $N_d < 30\ cm^{-3}$, Fig.2a). For lightly precipitating and non-precipitating clouds, LWP decreases with

757 N_d. The N_d-LWP relationship found in this study is consistent with that in Gryspeerdt et al. (2019) using global

758 mean cloud retrievals from MODIS and AMSR-E at coarser resolution of $1° \times 1°$ and daily timescale. This

759 consistency between different satellite measurements at different temporal and spatial scales greatly enhance our

760 confidence in the retrieved relationship.

761   This study further distinguishes non-precipitating clouds into thin and thick clouds based on their LWP. A

762 consistent decreasing trend in cloud water is found for both states, yet non-precipitating thick clouds exhibit more

763 negative LWP susceptibility ($\frac{dln(LWP)}{dln(N_d)} = -0.94$) compared to thin clouds ($\frac{dln(LWP)}{dln(N_d)} = -0.71$). The LWP

764 susceptibilities estimated in this study are more negative than those in Zhang et al. (2022) and Zhang and Feingold

765 (2023), based on similar classification of cloud states. Particularly, we found that non-precipitating thin clouds have

766 a decreasing trend in cloud water and a warming effect at the surface radiation while these are opposite in Zhang et

767 al. (2022) and Zhang and Feingold (2023). This is due to different seasons and study regions between our and their

768 studies. The summer boundary layer in the ENA region is deeper and less stable with higher cloud tops (e.g., Klein

769 and Hartmann, 1993; Ding et al., 2021; King et al., 2013) compared to the NE Pacific in Zhang et al. (2022) and the

770 NE Atlantic region in Zhang and Feingold (2023). The less stable condition, deeper boundary layer, and deeper

771 clouds could lead to a stronger cloud-top entrainment rate and result in a more negative LWP susceptibility (Possner

772 et al., 2020; Toll et al., 2019).

773   Regarding the CF adjustment to N_d perturbation, a daytime mean positive response is found for

774 precipitating and non-precipitating thin clouds and a negative response for non-precipitating thick clouds (Fig.2c).

775 Few studies have quantified the CF adjustment rate at 30-minute intervals for a direct comparison of CF

776 susceptibility. However, similar results are found using measurements and retrievals from different platforms at

777 various spatial and timescales, which greatly increase our confidence in the observed CF responses toward N_d

778 perturbation. For example, using MODIS measurement, Kaufman et al. (2005) found an increase in the longitudinal

779 mean cloudiness for warm boundary layer clouds with increasing AOD in all four regions of the Atlantic Ocean

780 characterized by distinct aerosol types. Using the natural experiment of volcanic eruption at Holuhraun in Iceland,

781 Chen et al. (2022) found that aerosols from the eruption increase the monthly mean cloud cover by 10% over the

782 North Atlantic. By tracking the cloud trajectory using geostationary satellites, Christensen et al. (2020) found that

783 aerosol enhance both CF and cloud lifetime in the timescale of 2-3 days, especially under stable conditions. It is

784 worth noting that a decrease in CF was not observed in these studies, likely due to the prevalence of non-

785 precipitating thin clouds and precipitating clouds in the Atlantic or the NE Pacific (e.g., Zhang and Feingold, 2023)

786 that mask the signal from non-precipitating thick clouds without distinguishing cloud states.

787   Lastly, the distinct "U-shaped" daytime variation in all three cloud properties found in this study (Fig.3a-c)

788 is *unlikely* due to the systematic bias in r_e and τ retrievals at large SZA based on the following two aspects. Firstly,

789 if the daytime variation is driven by retrieval bias at large SZA, we would expect the susceptibility exhibiting a

790 symmetric pattern at local noon. As shown in Figs. 10 and 6, the LWP and α_c susceptibilities for precipitating and

791 non-precipitating thick clouds exhibit asymmetric pattern at local noon: with a decreasing trend from 13 LST and a

792 daily minimum at 16 LST, and a continuously increasing trend from 11 to 18 LST, respectively. In addition, the CF

793 susceptibilities for all three cloud states show asymmetric patterns at local noon. Secondly, if the retrieval

794 uncertainty dominates the signal, we would expect less variation in cloud susceptibilities for overcast clouds, which

795 suffer less uncertainties in cloud retrievals from the plane-parallel assumption and the cloud 3-D effect. However,

796 the opposite is found from the sensitivity test where overcast clouds exhibit stronger daytime variation in cloud

797 susceptibilities (not shown).

798 **5. Conclusions**

799   Using N_d as an intermediary variable, this study investigates the aerosol indirect effect (AIE) for warm

800 boundary layer clouds and its daytime variation over the ENA region with the half-hourly and 3-km cloud property

801 retrievals from SEVIRI on the Meteosat-11. To constrain meteorological impacts on clouds and aerosol-cloud

802 interaction, cloud susceptibilities are estimated within a $1° \times 1°$ grid box for each satellite time step. Based on the

803 daytime mean cloud susceptibilities in the LWP-N_d parameter space, the sign and magnitude of cloud

804 susceptibilities strongly depend on the cloud states (Fig.2). Accordingly, warm boundary layer clouds are classified

805 into three states: precipitating clouds (r_e>15 μm), non-precipitating thick clouds (r_e<15 μm, LWP > 75 gm^{-2}), and

806 non-precipitating thin clouds (r_e<15 μm, LWP < 75 gm^{-2}).

807   Precipitating clouds exhibit contrasting responses in cloud LWP, with increases observed for heavily

808 precipitating clouds and decreases for lightly precipitating clouds. Positive α_c and CF susceptibilities are identified

809 for both heavily and lightly precipitating clouds. The net all-sky radiative forcing of the AIE on precipitating clouds

810 is estimated to be $-13\ W\ m^{-2} ln(N_d)^{-1}$, with contributions from the CF and α_c effects of -9.5 and -3.5

811 $W\ m^{-2}\ ln(N_d)^{-1}$, respectively. For non-precipitating clouds, both thick and thin clouds show negative LWP

812 susceptibility with more negative values found for thick clouds with higher LWP and N_d. This is likely attributed to

813 the stronger shortwave absorption, larger cloud top radiative cooling rate and stronger entrainment for thick clouds.

814 Consistent with the evaporation-entrainment feedback, non-precipitating thick clouds exhibit a decrease in CF and

815 α_c with increasing N_d, and results in a net warming effect at the surface and a radiative forcing of $+4.4$

816 $W\ m^{-2}\ ln(N_d)^{-1}$. On the other hand, non-precipitating thin clouds show an increasing response in CF and a less

817 negative α_c susceptibility. Additionally, the radiative effect from increasing CF $(-8.3\ W\ m^{-2}\ ln(N_d)^{-1})$ outweighs

818 that from a darker cloud $(+3.1\ W\ m^{-2} ln(N_d)^{-1})$ and leads to a net cooling effect of $-5.2\ W\ m^{-2}\ ln(N_d)^{-1}$.

819   Warm boundary layer clouds manifest distinct and significant ($p<0.05$) daytime variations in LWP, α_c, and

820 CF susceptibilities. All three cloud susceptibilities exhibit "U-shaped" diurnal patterns with clouds being less

821 susceptible in the morning and evening and more susceptible at local noon (Fig.3).

822   Daytime variation in LWP and α_c susceptibilities is likely attributed to the transition in cloud state while

823 clouds sustaining the memory of responses to N_d of the previous state (H1 in Table 1). From morning to noon, with

824 increasing solar radiation, non-precipitating thick clouds evolve to thin clouds. Thin clouds decayed from thick show

825 significantly more negative LWP and α_c susceptibilities than thin clouds that are previously thin (Fig.5). Therefore,

826 LWP and α_c susceptibilities decrease from morning to noon for thin clouds and reach their daily minima at noon

827 (Fig.4). In the afternoon, thin clouds develop to thick clouds while retaining the memory of less susceptible to N_d

828 perturbations (Fig.7) and therefore leads to an increase in LWP and α_c susceptibilities for nonprecipitating thick

829 clouds in the afternoon (Fig.6). Meanwhile, daytime variation in CF susceptibility for non-precipitating thick clouds

830 is more likely driven by changes in cloud morphology rather than the transition of cloud state (Fig.8, H3 in Table 1).

831 Compared to non-precipitating clouds, precipitating clouds exhibit smaller daytime variation in cloud susceptibility

832 (Fig.10).

833   The daytime variation in cloud susceptibility is primarily driven by changes in the intensity of cloud

834 susceptibilities from morning to noon, rather than changes in the frequency of occurrence of different cloud states

835 (Fig.12). As the polar-orbiting satellites only observe cloud susceptibilities across different cloud states during a

836 specific overpass time, they overlook the change in the intensity of cloud susceptibilities during the day. More

837 specifically, based on the daytime variation of cloud susceptibilities found in this study, LWP susceptibility

838 estimated at 13:30 LST could underestimate the daytime mean value by 26.3% (-0.76 compared to -0.60),

839 underestimate the α_c susceptibility by 475% (-0.023 compared to -0.004), and underestimate the CF susceptibility

840 by 120% (-0.019 compared to $+0.055$). It is worth noting that both the daytime variation and the daytime mean

841 values of cloud susceptibilities in this study are estimated based on the regression analysis on spatial data within

842 each satellite time step, with the assumption that the temporal change of cloud properties from N_d perturbations can

843 be represented by the spatial relationships.

844   This study underscores the importance of considering the diurnal cycle of cloud susceptibilities when

845 quantifying AIE and their impacts on clouds and radiation. The classification of cloud states enables us to

846 distinguish the sign, magnitude, and underlying processes driving the diurnal variation of AIE.

847   To further advance our understanding of the diurnal variation of AIE, several avenues for future research

848 can be pursued. Firstly, it is important to address uncertainties associated with satellite retrievals, which can

849 propagate into uncertainties in the retrieved N_d, as discussed in Grosvenor et al. (2018). Future study could utilize

850 active sensors to reduce these uncertainties, particularly during nighttime conditions. Moreover, using the retrieved

851 N_d as a proxy of aerosol concentration may introduce uncertainties related to cloud processes that can act as sources

852 or sinks of N_d, potentially buffer the relationships between N_d and cloud condensation nuclei. Future investigations

853 are needed to better understand the relationships, and how they vary with different cloud processes and throughout

854 the day. Lastly, this study encompasses all warm boundary layer clouds without considering the highly diverse

855 meteorological regimes and the associated cloud types in the ENA region. Classification of the synoptic and

856 meteorological conditions associated with different cloud states and aerosol properties would contribute to a more

857 comprehensive understanding, allowing for the disentanglement of the impacts of meteorology from AIE.

858

859

860 **Data availability:**

861 SEVIRI Meteosat-11 cloud retrieval products, produced by NASA LaRC SatCORPS group, are available from the

862 Atmospheric Radiation Measurement (ARM) Data Discovery website at https://adc.arm.gov/discovery/, Minnis

863 Cloud Products Using Visst Algorithm (visstgridm11minnis). The ARM ground-based radar and lidar observations

864 are available from ARM Data Discovery, KAZRARSCL, (arsclkazr1kollias).

865

879

Competing interests:

The authors declare that they have no conflict of interest.

882

883

References

Albrecht, B. A.: Aerosols, Cloud Microphysics, and Fractional Cloudiness, Science, 245, 1227–1230, https://doi.org/10.1126/science.245.4923.1227, 1989.

Arola, A., Lipponen, A., Kolmonen, P., Virtanen, T. H., Bellouin, N., Grosvenor, D. P., Gryspeerdt, E., Quaas, J., & Kokkola, H. (2022). Aerosol effects on clouds are concealed by natural cloud heterogeneity and satellite retrieval errors. Nature Communica)ons, 13(1), 7357. hrps://doi.org/10.1038/s41467-022-34948-5Bennartz, R.: Global assessment of marine boundary layer cloud droplet number concentration from satellite, J. Geophys. Res.,112, D02201, doi:10.1029/2006JD007547, 2007.

Bennartz, R. and Rausch, J.: Global and regional estimates of warm cloud droplet number concentration based on 13 years of AQUA-MODIS observations, Atmos. Chem. Phys., 17, 9815–9836, https://doi.org/10.5194/acp-17-9815-2017, 2017.

Bréon, F.-M., Tanré, D., and Generoso, S.: Aerosol effect on cloud droplet size monitored from satellite, Science, 295, 834–838, 2002.

Boers, R., and R. M. Mitchell: Absorption feedback in stratocumulus clouds: Influence on cloud top albedo. Tellus, 46A, 229–241, 1994.

Bretherton, C. S., Blossey, P. N., and Uchida, J.: Cloud droplet sedimentation, entrainment efficiency, and subtropical stratocumulus albedo, Geophys. Res. Lett., 34, L03813, https://doi.org/10.1029/2006GL027648, 2007.

Brenguier, J. L., Burnet, F., & Geoffroy, O.: Cloud optical thickness and liquid water path – does the coefficient vary with droplet concentration? *Atmospheric Chemistry and Physics*, *11*(18), 9771-9786. https://doi.org/10.5194/acp-11-9771-2011, 2011

Chen, Y.-C., Christensen, M., Stephens, G. L., and Seinfeld, J. H.: Satellite-based estimate of global aerosol–cloud radiative forcing by marine warm clouds, Nature Geosci., 7, 643–646, https://doi.org/10.1038/ngeo2214, 2014.

Chen, Y., Haywood, J., Wang, Y., Malavelle, F., Jordan, G., Partridge, D., Fieldsend, J., De Leeuw, J., Schmidt, A., Cho, N., Oreopoulos, L., Platnick, S., Grosvenor, D., Field, P., & Lohmann, U.: Machine learning reveals climate forcing from aerosols is dominated by increased cloud cover. *Nature Geoscience*, *15*(8), 609-614, 2022. https://doi.org/10.1038/s41561-022-00991-6

Christensen, M. W., Jones, W. K., and Stier, P.: Aerosols enhance cloud lifetime and brightness along the stratus-tocumulus transition, P. Natl. Acad. Sci. USA, 117, 17591–17598, https://doi.org/10.1073/pnas.1921231117, 2020.

Comstock, K. K., Wood, R., Yuter, S. E., and Bretherton, C. S.: Reflectivity and rain rate in and below drizzling stratocumulus, Q. J. Roy. Meteorol. Soc., 130, 2891–2918, doi:10.1256/qj.03.187, 2004.

Ding, F., Iredell, L., Theobald, M., Wei, J., & Meyer, D. :. PBL Height From AIRS, GPS RO, and MERRA-2 Products in NASA GES DISC and Their 10-Year Seasonal Mean Intercomparison. *Earth and Space Science*, *8*(9). https://doi.org/10.1029/2021ea001859, 2021

Dong, X., Xi, B., Kennedy, A., Minnis, P., & Wood, R.: A 19-month record of marine aerosol–cloud–radiation properties derived from DOE ARM mobile facility deployment at the Azores. Part I: Cloud fraction and single-

layered MBL cloud properties. Journal of Climate, 27(10), 3665–3682. https://doi.org/10.1175/JCLI-D-13-00553.1, 2014.

Dong, X., Xi, B., Qiu, S., Minnis, P., Sun-Mack, S., & Rose, F. : A radiation closure study of Arctic stratus cloud microphysical properties using the collocated satellite-surface data and Fu-Liou radiative transfer model. *Journal of Geophysical Research: Atmospheres*, *121*(17), 10,175-110,198. https://doi.org/10.1002/2016jd025255, 2016

Dong, X., Zheng, X., Xi, B., & Xie, S.: A Climatology of Midlatitude Maritime Cloud Fraction and Radiative Effect Derived from the ARM ENA Ground-Based Observations. Journal of Climate, 36(2), 531–546, https://doi.org/10.1175/JCLI-D-22-0290.1, 2023.

Duong, H. T., Sorooshian, A., and Feingold, G.: Investigating potential biases in observed and modeled metrics of aerosol-cloud precipitation interactions, Atmos. Chem. Phys., 11, 4027–4037, doi:10.5194/acp-11-4027-2011, 2011.

Fan, J. W., Wang, Y., Rosenfeld, D., and Liu, X. H.: Review of aerosol-cloud interactions: mechanisms, significance, and challenges, J. Atmos. Sci., 73, 4221–4252, 2016.

Feingold G, Eberhard W, Veron D, Previdi M. First measurements of the Twomey indirect effect using ground-based remote sensors. Geophys Res Lett. 30 (6). https://doi.org/10.1029/2002GL016633, 2003.

Feingold, G., Goren, T., & Yamaguchi, T. (2022). Quantifying albedo susceptibility biases in shallow clouds. Atmospheric Chemistry and Physics, 22(5), 3303–3319. https://doi.org/10.5194/acp-22-3303-2022.

Fons, E., Runge, J., Neubauer, D., & Lohmann, U.: Stratocumulus adjustments to aerosol perturbations disentangled with a causal approach. *npj Climate and Atmospheric Science*, *6*(1), 130, 2023

Glassmeier, F., Hoffmann, F., Johnson, J. S., Yamaguchi, T., Carslaw, K. S., and Feingold, G.: Aerosol-cloud-climate cooling overestimated by ship-track data, Science, 371, 485–489, https://doi.org/10.1126/science.abd3980, 2021.

Grosvenor, D. P., & Wood, R.: The effect of solar zenith angle on MODIS cloud optical and microphysical retrievals within marine liquid water clouds. *Atmospheric Chemistry and Physics*, *14*(14), 7291-7321. https://doi.org/10.5194/acp-14-7291-2014, 2014

Grosvenor, D. P., Sourdeval, O., Zuidema, P., Ackerman, A., Alexandrov, M. D., Bennartz, R., Boers, R., Cairns, B., Chiu, J. C., Christensen, M., Deneke, H., Diamond, M., Feingold, G., Fridlind, A., HÃOEnerbein, A., Knist, C., Kollias, P., Marshak, A., McCoy, D., Merk, D., Painemal, D., Rausch, J., Rosenfeld, D., Russchenberg, H., Seifert, P., Sinclair, K., Stier, P., van Diedenhoven, B., Wendisch, M., Werner, F., Wood, R., Zhang, Z., and Quaas, J.: Remote Sensing of Droplet Number Concentration in Warm Clouds: A Review of the Current State of Knowledge and Perspectives, Rev. Geophys., 56, 409–453, https://doi.org/10.1029/2017RG000593, 2018.

Gryspeerdt, E., Quaas, J., and Bellouin, N.: Constraining the aerosol influence on cloud fraction, J. Geophys. Res.-Atmos., 121, 3566–3583, https://doi.org/10.1002/2015JD023744, 2016.

Gryspeerdt, E., Goren, T., Sourdeval, O., Quaas, J., Mülmenst.dt, J., Dipu, S., Unglaub, C., Gettelman, A., and Christensen, M.: Constraining the aerosol influence on cloud liquid water path, Atmos. Chem. Phys., 19, 5331–5347, https://doi.org/10.5194/acp-19-5331-2019, 2019.

958 Gryspeerdt, E., Goren, T., and Smith, T. W. P.: Observing the timescales of aerosol–cloud interactions in snapshot
959   satellite images, Atmos. Chem. Phys., 21, 6093–6109, https://doi.org/10.5194/acp-21-6093-2021, 2021.

960 Gryspeerdt, E., McCoy, D. T., Crosbie, E., Moore, R. H., Nott, G. J., Painemal, D., Small-Griswold, J., Sorooshian,
961   A., and Ziemba, L.: The impact of sampling strategy on the cloud droplet number concentration estimated from
962   satellite data, Atmos.Meas. Tech., 15, 3875–3892, https://doi.org/10.5194/amt-15-3875-2022, 2022.

963 Han, Q., Rossow, W. B., Zeng, J., and Welch, R.: Three Different Behaviors of Liquid Water Path of Water Clouds
964   in Aerosol–Cloud Interactions, J. Atmos. Sci., 59, 726–735, https://doi.org/10.1175/1520-
965   0469(2002)059<0726:TDBOLW>2.0.CO;2, 2002.

966 Kaufman, Y. J., Koren, I., Remer, L. A., Rosenfeld, D., & Rudich, Y.: The effect of smoke, dust, and pollution
967   aerosol on shallow cloud development over the Atlantic Ocean. *Proc Natl Acad Sci U S A*, *102*(32), 11207-
968   11212. https://doi.org/10.1073/pnas.0505191102, 2005

969 King, M. D., Platnick, S., Menzel, W. P., Ackerman, S. A., & Hubanks, P. A.: Spatial and Temporal Distribution of
970   Clouds Observed by MODIS Onboard the Terra and Aqua Satellites. *IEEE Transactions on Geoscience and*
971   *Remote Sensing*, *51*(7), 3826-3852. https://doi.org/10.1109/tgrs.2012.2227333, 2013

972 Klein, S. A., & Hartmann, D. L.: The seasonal cycle of low stratiform clouds. Journal of Climate, 6(8), 1587–1606.
973   https://doi.org/10.1175/1520-0442(1993)006<1587:tscols>2.0.co;2, 1993.

974 Liu, J., Li, Z., and Cribb, M.: Response of marine boundary layer cloud properties to aerosol perturbations
975   associated with meteorological conditions from the 19-month AMF-Azores campaign, J. Atmos. Sci., 73, 4253–
976   4268, https://doi.org/10.1175/JAS-D- 15-0364.1, 2016.

977 Mather, J. H., & Voyles, J. W.: The Arm Climate Research Facility: A Review of Structure and Capabilities, *Bull.*
978   *Am. Meteorol. Soc.*, 94, 377-392, https://doi.org/10.1175/BAMS-D-11- 00218.1, 2013.

979 Mechem, D. B., Wittman, C. S., Miller, M. A., Yuter, S. E., and De Szoeke, S. P.: Joint synoptic and cloud
980   variability over the Northeast Atlantic near the Azores, J. Appl. Meteorol. Clim., 57, 1273–1290, 2018.

981 Minnis, P., Sun-Mack, S., Young, D. F., Heck, P. W., Garber, D. P., Chen, Y., Spangenberg, D. A., Arduini, R. F.,
982   Trepte, Q. Z., Smith, W. L., Ayers, J. K., Gibson, S. C., Miller, W. F., Hong, G., Chakrapani, V., Takano, Y.,
983   Liou, K., Xie, Y., and Yang, P.: CERES edition-2 cloud property retrievals using TRMM VIRS and Terra and
984   Aqua MODIS data–Part I: Algorithms, IEEE Trans. Geosci. Remote Sens., 49, 4374–4400,
985   https://doi.org/10.1109/TGRS.2011.2144601, 2011.

986 Minnis, P., K. Bedka, Q. Trepte, C. R. Yost, S. T. Bedka, B. Scarino, K. Khlopenkov, and M. M. Khaiyer: A
987   consistent long-term cloud and clear-sky radiation property dataset from the Advanced Very High Resolution
988   Radiometer (AVHRR). Climate Algorithm Theoretical Basis Document (C-ATBD), CDRP-ATBD-0826 Rev 1
989   - NASA, NOAA CDR Program, 159 pp., DOI:10.789/V5HT2M8T,
990   https://www1.ncdc.noaa.gov/pub/data/sds/cdr/CDRs/AVHRR_Cloud_Properties_NASA/AlgorithmDescription
991   _01B-30b.pdf, 2016.

992 Minnis, P., Sun-Mack, S., Chen, Y., Chang, F., Yost, C. R., Smith, W. L., Heck, P. W., Arduini, R. F., Bedka, S. T.,
993   Yi, Y., Hong, G., Jin, Z., Painemal, D., Palikonda, R., Scarino, B. R., Spangenberg, D. A., Smith, R. A., Trepte,

Q. Z., Yang, P., and Xie, Y.: CERES MODIS Cloud Product Retrievals for Edition 4–Part I: Algorithm

Changes, IEEE T. Geosci. Remote, 11152, 1–37, https://doi.org/10.1117/12.2532931, 2020.

Morrison, H., van Lier-Walqui, M., Fridlind, A. M., Grabowski, W. W., Harrington, J. Y., Hoose, C., et al.:

Confronting the challenge of modeling cloud and precipitation microphysics. Journal of Advances in Modeling

Earth Systems, 12, e2019MS001689. https://doi.org/10.1029/2019MS001689, 2020.

Painemal, D., Minnis, P., and Sun-Mack, S.: The impact of horizontal heterogeneities, cloud fraction, and liquid

water path on warm cloud effective radii from CERES-like Aqua MODIS retrievals, Atmos. Chem. Phys., 13,

9997–10003, https://doi.org/10.5194/acp-13-9997-2013, 2013.

Painemal, D.: Global Estimates of Changes in Shortwave Low-Cloud Albedo and Fluxes Due to Variations in Cloud

Droplet Number Concentration Derived From CERES-MODIS Satellite Sensors, Geophys. Res. Lett., 45,

9288–9296, https://doi.org/10.1029/2018GL078880, 2018.

Painemal, D., Spangenberg, D., Smith Jr.,W. L., Minnis, P., Cairns, B., Moore, R. H., Crosbie, E., Robinson, C.,

Thornhill, K. L., Winstead, E. L., and Ziemba, L.: Evaluation of satellite retrievals of liquid clouds from the

GOES-13 imager and MODIS over the midlatitude North Atlantic during the NAAMES campaign, Atmos.

Meas. Tech., 14, 6633–6646, https://doi.org/10.5194/amt-14-6633-2021, 2021.

Penner, J. E., Dong, X., and Chen, Y.: Observational evidence of a change in radiative forcing due to the indirect

aerosol effect, Nature, 427, 231–234, 2004.

Petters, J. L., J. Y. Harrington, and E. E. Clothiaux: Radiative–Dynamical Feedbacks in Low Liquid Water Path

Stratiform Clouds. J. Atmos. Sci., 69, 1498–1512, https://doi.org/10.1175/JAS-D-11-0169.1, 2012.

Possner, A., Eastman, R., Bender, F., & Glassmeier, F.: Deconvolution of boundary layer depth and aerosol

constraints on cloud water path in subtropical stratocumulus decks. *Atmospheric Chemistry and Physics*, *20*(6),

3609-3621. https://doi.org/10.5194/acp-20-3609-2020, 2020

Rémillard, J., Kollias, P., Luke, E., and Wood, R.: Marine Boundary Layer Cloud Observations in the Azores, J.

Climate, 25, 7381–7398, https://doi.org/10.1175/JCLI-D-11-00610.1, 2012.

Sandu, I., Brenguier, J., Geoffroy, O., Thouron, O., and Masson, V.: Aerosol impacts on the diurnal cycle of marine

stratocumulus, J. Atmos. Sci., 65, 2705–2718, 2008.

Sandu, I., Brenguier, J.-L., Thouron, O., and Stevens, B.: How important is the vertical structure for the

representation of aerosol impacts on the diurnal cycle of marine stratocumulus? Atmos. Chem. Phys., 9, 4039–

4052, doi:10.5194/acp-9-4039-2009, 2009.

Sato, Y., Goto, D., Michibata, T., Suzuki, K., Takemura, T., Tomita, H., and Nakajima, T.: Aerosol effects on cloud

water amounts were successfully simulated by a global cloud-system resolving model, Nat. Commun., 9, 985,

https://doi.org/10.1038/s41467-018-03379-6, 2018.

Small, J., Chuang, P., Feingold, G. & Jiang, H.: Can aerosol decrease cloud lifetime? Geophys. Res. Lett. 36,

L16806, 2009.

Stevens, B. and Feingold, G.: Untangling aerosol effects on clouds and precipitation in a buffered system, Nature,

461, 607–613, doi:10.1038/nature08281, 2009.

Stevens, B. & Seifert, A.: Understanding the macrophysical outcomes of microphysical choices in simulations of shallow cumulus convection. J. Meteorol. Soc. Jpn 86A, 141–163, 2008.

Sun-Mack, S., Minnis, P., Chen, Y., Kato, S., Yi, Y., Gibson, S. C., et al.: Regional apparent boundary layer lapse rates determined from CALIPSO and MODIS data for cloud-height determination. Journal of Applied Meteorology and Climatology, 53(4), 990–1011, 2014.

Terai, C. R., Wood, R., Leon, D. C., and Zuidema, P.: Does precipitation susceptibility vary with increasing cloud thickness in marine stratocumulus? Atmos. Chem. Phys., 12, 4567–4583, doi:10.5194/acp-12-4567-2012, 2012.

Terai, C. R., Wood, R., and Kubar, T. L.: Satellite estimates of precipitation susceptibility in low-level marine stratiform clouds, J. Geophys. Res., 120, 8878–8889, doi:10.1002/2015JD023319, 2015.

Toll, V., Christensen, M., Quaas, J., and Bellouin, N.: Weak average liquid-cloud-water response to anthropogenic aerosols, Nature, 572, 51–55, https://doi.org/10.1038/s41586-019-1423-9, 2019.

Trepte, Q. Z., and Coauthors: Global cloud detection for CERES edition 4 using Terra and Aqua MODIS data. IEEE Trans. Geosci. Remote Sens., 57, 9410–9449, https://doi.org/10.1109/TGRS.2019.2926620, 2019.

Twomey, S.: The Influence of Pollution on the Shortwave Albedo of Clouds, J. Atmos. Sci., 34, 1149–1152, https://doi.org/10.1175/1520-0469(1977)034<1149:TIOPOT>2.0.CO;2, 1977.

Wang, S., Wang, Q., and Feingold, G.: Turbulence, Condensation, and Liquid Water Transport in Numerically Simulated Nonprecipitating Stratocumulus Clouds, J. Atmos. Sci., 60, 262–278, https://doi.org/10.1175/1520-0469(2003)060<0262:TCALWT>2.0.CO;2, 2003.

Wang, Y., Zheng, X., Dong, X., Xi, B.,Wu, P., Logan, T., and Yung, Y. L.: Impacts of long-range transport of aerosols on marineboundary-layer clouds in the eastern North Atlantic, Atmos. Chem. Phys., 20, 14741–14755, https://doi.org/10.5194/acp-20-14741-2020, 2020.

Warren, S. G., C. J. Hahn, J. London, R. M. Chervine, and R. L. Jenne: Global distribution of total cloud cover and cloud type amounts over ocean, Tech. Note NCAR/TN-317 + STR, 42, Natl. Cent. for Atmos. Res., Boulder, Colo., https://doi.org/10.2172/5415329, 1988.

Williams, A. S., & Igel, A. L.: Cloud top radiative cooling rate drives non-precipitating stratiform cloud responses to aerosol concentration. Geophysical Research Letters, 48, e2021GL094740. https://doi.org/10.1029/2021GL094740, 2021.

Wood, R.: Stratocumulus Clouds, Mon. Weather Rev., 140, 2373–2423, https://doi.org/10.1175/MWR-D-11-00121.1, 2012.

Wu, P., Dong, X., Xi, B., Tian, J., & Ward, D. M.: Profiles of MBL cloud and drizzle microphysical properties retrieved from ground-based observations and validated by aircraft in situ measurements over the Azores. Journal of Geophysical Research: Atmospheres, 125, e2019JD032205. https://doi.org/10.1029/2019JD032205, 2020.

Wu, P., X. Dong, and B. Xi: A climatology of marine boundary layer cloud and drizzle properties derived from ground-based observations over the Azores. J. Climate, 33, 10133–10148, https://doi.org/10.1175/JCLI-D-20-0272.1, 2020.

Xi, B., Dong, X., Minnis, P., & Khaiyer, M. M.: A 10 year climatology of cloud fraction and vertical distribution derived from both surface and GOES observations over the DOE ARM SPG site. *Journal of Geophysical Research*, *115*(D12). https://doi.org/10.1029/2009jd012800, 2010

Xue, H. and Feingold, G.: Large-Eddy Simulations of Trade Wind Cumuli: Investigation of Aerosol Indirect Effects, J. Atmos. Sci., 63, 1605–1622, https://doi.org/10.1175/JAS3706.1, 2006.

Yeom, J. M., Yum, S. S., Shaw, R. A., La, I., Wang, J., Lu, C., et al.: Vertical variations of cloud microphysical relationships in marine stratocumulus clouds observed during the ACE ENA campaign. Journal of Geophysical Research: Atmospheres, 126, e2021JD034700. https://doi.org/10.1029/2021JD034700, 2021.

Zhang, Z., Song, Q., Mechem, D. B., Larson, V. E., Wang, J., Liu, Y., Witte, M. K., Dong, X., and Wu, P.: Vertical dependence of horizontal variation of cloud microphysics: observations from the ACE-ENA field campaign and implications for warm-rain simulation in climate models, Atmos. Chem. Phys., 21, 3103–3121, https://doi.org/10.5194/acp-21-3103-2021, 2021.

Zhang, J., Zhou, X., Goren, T., and Feingold, G.: Albedo susceptibility of northeastern Pacific stratocumulus: the role of covarying meteorological conditions, Atmos. Chem. Phys., 22, 861–880, https://doi.org/10.5194/acp-22-861-2022, 2022.

Zhang, J., and Feingold, G.: Distinct regional meteorological influences on low-cloud albedo susceptibility over global marine stratocumulus regions, Atmos. Chem. Phys., 23, 1073–1090, https://doi.org/10.5194/acp-23-1073-2023, 2023.

Zheng, Q., and Miller, M. A.: Summertime Marine Boundary Layer Cloud, Thermodynamic, and Drizzle Morphology over the Eastern North Atlantic: A Four-Year Study, J. Climate, 35, 4805-4825, https://doi.org/10.1175/JCLI-D-21-0568.1, 2022.

Zheng, X. J., B. K. Xi, X. Q. Dong, P. Wu, T. Logan, and Y. Wang, 2022: Environmental effects on aerosol–cloud interaction in non-precipitating marine boundary layer (MBL) clouds over the eastern North Atlantic. Atmospheric Chemistry and Physics, 22, 335−354, https://doi.org/10.5194/acp-22-335-2022.

Zhou, X., Zhang, J., & Feingold, G.: On the importance of sea surface temperature for aerosol-induced brightening of marine clouds and implications for cloud feedback in a future warmer climate. Geophysical Research Letters, 48, e2021GL095896. https://doi org/10.1029/2021GL095896, 2021.

Zhou, X., & Feingold, G. (2023). Impacts of mesoscale cloud organization on aerosol-induced cloud water adjustment and cloud brightness. Geophysical Research Letters, 50, e2023GL103417. https://doi.org/10.1029/2023GL103417

Zuidema, P., Leon, D., Pazmany, A., & Cadeddu, M.: Aircraft millimeter-wave passive sensing of cloud liquid water and water vapor during VOCALS-REx. *Atmospheric Chemistry and Physics*, *12*(1), 355-369. https://doi.org/10.5194/acp-12-355-2012, 2012